An orally bioavailable SARS-CoV-2 main protease inhibitor exhibits improved affinity and reduced sensitivity to mutations

Michael Westberg[1,2,3,*], **Yichi Su**[1,4], **Xinzhi Zou**[5], **Pinghan Huang**[6], **Arjun Rustagi**[7], **Jaishree Garhyan**[8], **Puja Bhavesh Patel**[8], **Daniel Fernandez**[9,10], **Yan Wu**[5], **Chenzhou Hao**[1], **Chieh-Wen Lo**[7], **Marwah Karim**[7], **Lin Ning**[1], **Aimee Beck**[7], **Panatda Saenkham-Huntsinger**[6], **Vivian Tat**[11], **Aleksandra Drelich**[6], **Bi-Hung Peng**[12], **Shirit Einav**[7,13,14], **Chien-Te K. Tseng**[6,11,12], **Catherine Blish**[7,14], **Michael Z. Lin**[1,5,15,*]

[1]Department of Neurobiology, Stanford University; Stanford, CA 94305, USA.

[2]Department of Chemistry, Aarhus University; 8000 Aarhus C, Denmark.

[3]Interdisciplinary Nanoscience Center (iNANO), Aarhus University; 8000 Aarhus C, Denmark.

[4]Institute for Translational Brain Research, State Key Laboratory of Medical Neurobiology, MOE Frontiers Center for Brain Science, Fudan University, Shanghai, 200032, China.

[5]Department of Bioengineering, Stanford University; Stanford, CA 94305, USA.

[6]Department of Microbiology and Immunology, The University of Texas Medical Branch; Galveston, TX 77555, USA.

[7]Department of Medicine, Stanford University; Stanford, CA 94305, USA.

[8]Stanford In Vitro Biosafety Level 3 Service Center, Stanford University; Stanford, CA 94305, USA.

[9]Program in Chemistry, Engineering, and Medicine for Human Health (ChEM-H), Stanford University; Stanford, CA 94305, USA.

[10]Sarafan ChEM-H, Macromolecular Structure Knowledge Center, Stanford University; Stanford, CA 94305, USA.

[11]Department of Pathology, The University of Texas Medical Branch; Galveston, TX 77555, USA.

[12]Department of Neuroscience, Cell Biology, and Anatomy, The University of Texas Medical Branch; Galveston, TX 77555, USA.

[13]Department of Microbiology and Immunology, Stanford University; Stanford, CA 94305, USA

[*]Corresponding authors. westberg@chem.au.dk, mzlin@stanford.edu.

Author contributions:

MW and MZL conceptualized the study. MW, YS, XZ, AR, PH, JG, DF, C-WL, MK, LN, AB, B-HP, SE, C-TKT, CB, and MZL developed the methodology. MW, YS, XZ, AR, PH, JG, PBP, DF, YW, CH, C-WL, MK, LN, AB, PS-H, VT, AD, and B-HP performed the investigation. MW and MZL visualized the data. MW, JG, SE, C-TKT, CB, and MZL supervised the study. MW wrote the original draft of the manuscript. MW and MZL reviewed and edited the manuscript.

Competing interests: MZL, MW, YS, XZ, and LN are co-inventors on patent application WO 2021/226546 A1 PROTEASE INHIBITORS FOR TREATMENT OR PREVENTION OF CORONAVIRUS DISEASE. MZL, MW, and YS are co-inventors on patent application WO 2023/114516 A2 CELL-PERMEANT INHIBITORS OF VIRAL CYSTEINE PROTEASES. These patent applications describe compounds developed in this study.

[14]Chan Zuckerberg Biohub; San Francisco, CA 94158, USA.

[15]Department of Chemical and Systems Biology, Stanford University; Stanford, CA 94305, USA.

Abstract

Inhibitors of the severe acute respiratory syndrome coronavirus 2 (SARS-CoV-2) main protease (M^{pro}) such as nirmatrelvir (NTV) and ensitrelvir (ETV) have proven effective in reducing the severity of COVID-19, but the presence of resistance-conferring mutations in sequenced viral genomes raises concerns about future drug resistance. Second-generation oral drugs that retain function against these mutants are thus urgently needed. We hypothesized that the covalent hepatitis C virus (HCV) protease inhibitor boceprevir (BPV) could serve as the basis for orally bioavailable drugs that inhibit SARS-CoV-2 M^{pro} more efficiently than existing drugs. Performing structure-guided modifications of BPV, we developed a picomolar-affinity inhibitor, ML2006a4, with antiviral activity, oral pharmacokinetics, and therapeutic efficacy similar or superior to NTV. A crucial feature of ML2006a4 is a derivatization of the ketoamide reactive group that improves cell permeability and oral bioavailability. Finally, ML2006a4 was found to be less sensitive to several mutations that cause resistance to NTV or ETV and occur in the natural SARS-CoV-2 population. Thus, anticipatory design can preemptively address potential resistance mechanisms to expand future treatment options against coronavirus variants.

One Sentence Summary:

ML2006a4 has improved affinity for SARS-CoV-2 M^{pro} and reduced sensitivity to mutations conferring resistance to nirmatrelvir or ensitrelvir.

INTRODUCTION

In the last two decades, three coronaviruses have emerged from animal reservoirs to cause lethal respiratory illnesses in humans. In particular, more than 7 million people have already died from coronavirus disease 2019 (COVID-19) caused by SARS-CoV-2 (1). Although immunity from infection or vaccination greatly reduces the risk of death (2, 3), the high prevalence and intrinsic virulence of SARS-CoV-2 continue to cause morbidity and mortality. In addition, SARS-CoV-2 has repeatedly evolved to evade existing immunity. Thus, oral anti-coronavirus drugs that can prevent progression to severe disease remain necessary.

The coronavirus main protease (M^{pro}) is essential for viral replication and a major target for antiviral drugs (4–6). Prior to SARS-CoV-2 emergence, experimental inhibitors of M^{pro} were found to protect mice and cats from lethal disease caused by coronaviruses (7–9). The SARS-CoV-2 M^{pro} inhibitor nirmatrelvir (NTV) (10) was proven to reduce hospitalization risk by 89% in unvaccinated COVID-19 patients (11), leading to its emergency approval and later full approval in multiple countries (12). A non-covalent non-peptidomimetic M^{pro} inhibitor, ensitrelvir (ETV) (13), has also shown clinical efficacy and is approved for use in Japan (14–16). In China, leritrelvir (17, 18) and simnotrelvir (19, 20) have been conditionally approved. Additional oral M^{pro} inhibitors have entered clinical trials (21),

but molecular structures have only been disclosed for pomotrelvir (PTV) (22), ibuzatrelvir, and olgotrelvir (23), and the published data are overall sparse for all these inhibitors. Nevertheless, the success of NTV and ETV demonstrate the utility of targeting M^{pro} to treat coronavirus-driven disease.

A major concern, however, is the potential for emergence of drug-resistant SARS-CoV-2 mutants. Genomic surveillance of SARS-CoV-2 has been performed on a large scale since the beginning of the pandemic, enabling the detection of new alleles while they are still rare (24–30). This may guide the preemptive development of new drugs to address mutants that resist available treatments. Examples of concerning M^{pro} mutations detected by genomic surveillance and laboratory experiments are S144A, E166X, and A173V, which decrease NTV or ETV potency while maintaining viable virus replication (16, 24, 25, 31–49).

One drug design strategy to reduce the risk of resistance is to mimic the interactions of the substrate to conserved atoms of the enzyme (50). Such substrate mimicry reduces the risk of escape mutations in M^{pro}, as mutations that affect inhibitor binding will also affect substrate binding and thereby viral fitness. Thus, designing strong interactions between drugs and essential active site residues of M^{pro} should both maximize inhibition and minimize the risk of escape mutants.

NTV is a covalent M^{pro} inhibitor, using a nitrile as an electrophilic group (or “warhead”) to react with the nucleophilic C145 in the active site (10). Prior to NTV, the only warhead used in approved viral protease inhibitors was the ketoamide group of the HCV drugs telaprevir (TPV), boceprevir (BPV), and narlaprevir (NPV). These drugs are orally bioavailable and safe, even when taken continuously for more than 6 months (51, 52). In addition, ketoamides form stable adducts mimicking the tetrahedral transition states and hemiketal/hemithioketal intermediates of substrate proteolysis (53–55). Indeed, a series of ketoamide-based inhibitors developed for SARS-CoV-1 M^{pro}, culminating in 13b, were shown to be active against SARS-CoV-2 M^{pro} (56, 57). However, 13b demonstrates a relatively high 50% effective antiviral concentration (EC_{50}) of about 5 μM (57), compared to about 0.1 μM for NTV (10). Another noteworthy class of reversible covalent inhibitors are aldehydes or their prodrugs, such as GC376 (6, 23, 58–60). However, aldehydes are considered non-ideal drug candidates due to their metabolic instability, low oral bioavailability, and toxicity caused by off-target reactions (61, 62).

In this study, we address the questions of whether ketoamide-based M^{pro} inhibitors can be designed with similar potency as NTV, and if they can be effective against NTV- or ETV-resistant mutants. We hypothesized that BPV supplies a preorganized scaffold for the generation of robust M^{pro} inhibitors. Our first compound based on this hypothesis, ML1000, efficiently inhibited SARS-CoV-2 M^{pro} with a 50% inhibitory concentration (IC_{50}) of 20 nM, but was limited in permeability. We performed structure-guided modifications on side groups and on the ketoamide warhead to improve affinity and permeability. The resulting lead compound, ML2006a4, is a picomolar-affinity inhibitor with oral pharmacokinetics and antiviral efficacy in mice similar or superior to NTV. ML2006a4 binding to M^{pro} is impacted

to a lesser degree by several mutations that reduce potency of NTV or ETV, suggesting it may be useful if resistance to these M^{pro} inhibitors arises.

RESULTS

HCV protease inhibitors show activity against M^{pro}.

At the onset of the SARS-CoV-2 pandemic, we asked whether HCV protease inhibitors could be repurposed to inhibit M^{pro}. We manually docked BPV into the SARS-CoV-2 M^{pro} active site, observing good shape complementarity by its P1, P2, and P4 groups (Fig. 1A). The bicyclic P2 proline analogue in BPV filled the deep S2 pocket in M^{pro}, and its backbone φ and ψ angles retraced those of the P2 Leu or Phe residues of earlier M^{pro} inhibitors (57, 63) (Fig. 1A and fig. S1). The distinct bicyclic proline analogue of TPV could also fill S2 while retracing the M^{pro} inhibitor backbone conformation (fig. S1). The P3-analogous t-butyl group of BPV, TPV, and NPV also mimicked the outward orientation of the P3 group of M^{pro} substrates (64), but the P4 group of BPV, but not of TPV or NPV, was small enough to fit into the S4 pocket (fig. S1). Thus, we hypothesized that BPV and, to a lesser extent, NPV and TPV, may be able to inhibit M^{pro}. After finding that BPV and TPV inhibited M^{pro} in mammalian cells and enzymatic assays (fig. S2), we measured IC_{50} values for BPV, TPV, NPV, and other proposed M^{pro} inhibitors (fig. S3). BPV, TPV, and NPV all showed activity against M^{pro}, with BPV being the most potent (IC_{50} = 6.2 μM). During the course of this work, at least three other groups reported BPV inhibiting SARS-CoV-2 M^{pro} at low micromolar concentrations (65–67).

A lead inhibitor was derived from boceprevir.

We next designed inhibitors combining the bicyclic P2 rings of BPV or TPV with side groups optimized for M^{pro} binding. Gln at P1 is strongly preferred by all coronavirus M^{pro} species (68). This preference is conserved in the related enterovirus 3C proteases, such as human rhinovirus (HRV) protease (69). Beginning with the HRV protease inhibitor rupintrivir, enterovirus and coronavirus protease inhibitors have incorporated a γ- or δ-lactam group at P1 as a Gln mimic (70–72). We initially designed two compounds with a γ-lactam at P1 and a bicyclic ring at P2: ML1000, with the P2, P3, P4, and ketoamide groups of BPV, and similarly ML1100 but with the P2 group of TPV (Fig. 1B). We retained the P3 t-butyl of BPV/TPV, as it was preferred at this position in substrate screens (73), and as its lipophilicity could aid permeability.

ML1000 and ML1100 were potent M^{pro} inhibitors in solution, with measurable IC_{50} values limited by the 100 nM M^{pro} concentrations required to detect activity. To maintain M^{pro} activity at low nanomolar concentrations, we engineered a M^{pro}-coil fusion protein for avidity-enhanced dimerization and thereby measurable activity at 1 nM. In this assay, ML1000 and ML1100 produced IC_{50} values of 20 nM and 67 nM, respectively (Fig. 1C and fig. S4). A ML1000-M^{pro} crystal structure confirmed the P1 γ-lactam was positioned

similarly to other M^{pro} inhibitors, with the other atoms matching the manually docked BPV structure (Fig. 1D).

However, ML1000 and ML1100 incorporate 6 H-bond donors (HBDs) and 6 H-bond acceptors (HBAs), an unfavorable number for membrane permeability (74). Indeed, their apparent permeability (P_{app}) in Caco-2 cell layers was low (table S1), and they failed to inhibit SARS-CoV-2 replication even at 100 μM (fig. S5 and S6). Nevertheless, we hypothesized the ketoamide-based inhibitors would be useful for maximizing drug-target interactions, as the warhead allows P1' extensions and, after reaction, mimics the tetrahedral transition state and hemithioketal substrate intermediate with multiple H-bonds to M^{pro} (Fig. 1D). Thus, we chose ML1000 as a lead compound for developing high-affinity oral M^{pro} inhibitors that are robust to mutation.

Lead optimization improved permeability and potency.

We performed stepwise optimization of ML1000 to improve permeability and potency (Fig. 2, A and B). To aid in drug screening, we devised a bioluminescent measurement of intracellular inhibition of M^{pro} (IC_{50}). In this assay, M^{pro} activity eliminates a luciferase reporter, such that M^{pro} inhibition increases luminescence (fig. S7). We used higher $IC_{50}/IC_{50,cell}$ ratios to identify more permeable drugs.

First, we exchanged the rigid and bulky urea of ML1000 (fig. S8) for an amide with various alkyl groups, removing a HBD and optimizing the fit of P4, in ML1001 through ML1003 (Fig. 2A). ML1001 exhibited the lowest IC_{50}, but $IC_{50,cell}$ and antiviral EC_{50} remained high (Fig. 2C). Second, to better mimic P1' substrate interactions and improve permeability, we replaced a ketoamide hydrogen in ML1001 and ML1002 with N-methyl, creating ML1001m and ML1002m. Although this lowered IC_{50}, suggesting favorable interactions between the methyl group and the S1' pocket, it did not improve $IC_{50,cell}$ or antiviral EC_{50} (Fig. 2C).

Third, we shrunk P4, as the ML1001-M^{pro} crystal structure revealed the P4 group was not fully buried inside the S4 pocket (Fig. 2D). We synthesized ML1004m through ML1006m with methyl, difluoromethyl, and trifluoromethyl P4 groups (Fig. 2, A and B). As a benchmark, we also synthesized NTV, which at this time in our study was revealed to be identical to ML1001 in P1, P2, and P3 (10). Difluoromethyl and trifluoromethyl groups (ML1005m and ML1006m) produced IC_{50} values of 3.4 and 3.6 nM, respectively, lower than the 11 nM of the methyl (ML1004m) (Fig. 2C). ML1006m showed the lowest $IC_{50,cell}$, but antiviral EC_{50} remained > 4 μM (Fig. 2C).

Fourth, we removed all ketoamide HBDs to boost permeability. As a ML1006m-M^{pro} crystal structure revealed limited space around the ketoamide (Fig. 2E), we explored small substitutions (Fig. 2A). ML1006d contains a *N,N*-dimethylketoamide, but IC_{50} increased to 138 nM (Fig. 2F), possibly due to methyl-carbonyl intramolecular clashes and associated twisting within the ketoamide (75, 76). ML1006a, in which we designed a strained four-membered azetidine ring as a compact non-clashing *N,N*-substitution, maintained an IC_{50} of 2.9 nM (Fig. 2F). ML1006a achieved antiviral EC_{50} of 0.68 μM, a clear improvement

over ML1006m (Fig. 2G), but still inferior to NTV. A ML1006a-M^{pro} structure revealed the expected planar azetidinyl ketoamide in the S1' pocket (Fig. 2H).

Fifth, we remodified P1 to improve lipophilicity. ML2006a enlarged P1 into a δ-lactam as in some earlier protease inhibitors (71, 77–79), while ML3006a and ML4006a incorporated "inverted lactams" to remove a HBD (Fig. 3A). ML2006a improved on IC_{50}, $IC_{50,cell}$ and antiviral EC_{50} (Fig. 3, B and C, and fig. S9). ML3006a and ML4006a were more permeable based on the $IC_{50}/IC_{50,cell}$ ratio and P_{app} measurements (Fig. 3C and table S1), but IC_{50}, $IC_{50,cell}$, and EC_{50} were increased (Fig. 3, B and C), as expected from removing a H-bond with E166 (fig. S10).

In a final step to improve lipophilicity, we tested difluoro and dimethyl 3,3-substitutions of the azetidine of ML2006a, creating ML2006a2 and ML2006a4 (Fig. 3A). The larger 3,3-dimethyl azetidinyl of ML2006a4 is just contained within S1' (Fig. 3D and fig. S10). These compounds retained the low IC_{50} and $IC_{50,cell}$ of ML2006a (Fig. 3, C to E) while improving permeability (Fig. 3C and table S1). ML2006a, ML2006a2, and ML2006a4 achieved antiviral EC_{50} values of 100 to 120 nM in Huh7.5.1-ACE2-TMPRSS2 (Huh7.5.1++) cells, lower than the 190 nM of NTV (Fig. 3C and F). In A549-ACE2 (A549+) and Calu-3 cells, their EC_{50} values were similar to NTV (Fig. 3C and fig. S11).

ML2006a4 is orally bioavailable in mice.

We performed in vitro absorption, distribution, metabolism and excretion (ADME) assays at several steps during inhibitor optimization. Like NTV (10), the ketoamide-based inhibitors also undergo degradation by CYP3A, an effect counteracted by ritonavir (RTV) (table S1). We measured pharmacokinetics (PK) in mice for ML1006m, ML1006a, ML2006a, ML2006a4, and NTV (Fig. 4, A and B), all formulated in a saline solution with PEG-300, DMSO, and Tween-80 (PDT formulation). As expected, pre-dosing of RTV lowers clearance of all five compounds. Oral bioavailability (F) improves throughout the ketoamide series, culminating with 27% or 115% for ML2006a4 without or with RTV, respectively. Although ML2006a2 has antiviral potency and in vitro ADME properties comparable to ML2006a4, including human microsome and plasma stability, its low stability in mouse plasma precluded in vivo characterization (table S1). When dosed orally at 20 mg/kg with RTV in PDT, mouse plasma concentrations of NTV and ML2006a4 exceeded plasma protein binding-adjusted antiviral EC_{90} and EC_{50} ($EC_{90,p}$ and $EC_{50,p}$) values for approximately 8 h and 12 h after administration, respectively (Fig. 4B).

As NTV demonstrated initial evidence of efficacy in mice at a high dose without RTV (10), we also asked how ML2006a4 would compare to NTV in PK with a high-dose single-agent regimen. When administered orally at 300 mg/kg in aqueous suspensions with methylcellulose and Tween-80, conditions similar to those used previously for NTV (10), mouse plasma concentrations of ML2006a4 and NTV were comparable at most time points (Fig. 4C).

We also obtained ADME and PK data for PTV, a nitrile-based M^{pro} inhibitor that was recently tested in humans as a RTV-free COVID-19 treatment but failed to achieve the

clinical endpoints. The clearance of PTV by human liver microsomes was higher than that of NTV or ML2006a4, suggesting that PTV is not better suited for a single-agent regimen than NTV or ML2006a4 (table S1). In addition, metabolism of PTV was only partly suppressed by RTV (table S1), indicating that enzymes beyond CYP3A contribute to its degradation. In mice, total plasma concentrations of PTV closely matched NTV and ML2006a4 when dosed orally with RTV at 20+20 mg/kg in the PDT formulation (Fig. 4B). However, due to a high degree of plasma protein binding (table S1), the $EC_{50,p}$ is substantially higher for PTV than for NTV and ML2006a4, leading to rapid decay to plasma concentrations below $EC_{50,p}$ (Fig. 4B). In addition, when administered at 300 mg/kg without RTV, PTV plasma concentrations were lower than those of NTV and ML2006a4, and dropped below $EC_{50,p}$ after 1 h (Fig. 4C). Thus, our data indicates that PTV is an inferior SARS-CoV-2 antiviral compared to NTV and ML2006a4 either with or without RTV.

ML2006a4 rescues SARS-CoV-2 infected mice.

Having identified ML2006a4 as the lead compound with the most favorable PK, we assessed its toxicity in vitro and in vivo. In cytotoxicity tests, ML2006a4 demonstrated 50% cytotoxicity concentrations (CC_{50}) > 100 μM (table S2). We then compared the tolerability of ML2006a4 and NTV in mice. Protease inhibitors (40 mg/kg) and RTV (20 mg/kg) were orally administered twice daily (po bid) as a co-suspension in 0.5% methylcellulose and 2% Tween-80 (MCT-2). This dosing regimen was chosen to simulate the human equivalent dose of NTV, and it maintained plasma concentrations at or above $EC_{50,p}$ for about 6 h (Fig. 5A and fig. S12). All groups gained weight similarly over the 4 days with no clinical abnormalities (fig. S12). Whereas no systematic biochemical or hematological abnormalities were observed for the ML2006a4+RTV combination, NTV+RTV induced elevated liver enzymes in 3 of 6 mice (tables S3 and S4). Reversible liver changes and increased concentrations of alanine aminotransferase and aspartate aminotransferase have previously been observed in NTV-dosed rats and monkeys, but have not been observed in humans clinical studies (80). Overall, 40+20 mg/kg of ML2006a4+RTV in MCT-2 appeared at least as safe as NTV+RTV at similar doses and was used for the subsequent efficacy study.

To assess the in vivo therapeutic efficacy of ML2006a4, 16-week-old BALB/c mice were infected with mouse-adapted SARS-CoV-2 MA10, and drugs were administered po bid for 4 days (Fig. 5B). Within 5 days post infection (dpi), SARS-CoV-2 MA10 was lethal to all mice in the RTV-only control group, whereas administration of NTV+RTV or ML2006a4+RTV fully rescued the infected mice and ensured minimal weight loss and no clinical abnormalities (Fig. 5, C and D). Viral titers and viral RNA load in lung tissues were determined at 2 dpi and at the end of the study (terminal or 6 dpi). At both timepoints, ML2006a4+RTV or NTV+RTV showed reductions in infectious viral titers compared to RTV alone (Fig. 5E). Further, at 6 dpi, the viral RNA load was significantly ($p = 0.025$) lower in ML2006a4-treated mice than in NTV-treated mice, although a significant difference was not observed in infectious viral titers (Fig. 5, E and F). Histopathological evaluation of the NTV-treated group revealed a high extent of infiltrations and severe injury in respiratory epithelia at 2 dpi followed by incomplete epithelial regeneration at 6 dpi. In contrast, the ML2006a4-treated group showed minimal epithelial injury at 2 dpi and rapid regeneration at

6 dpi (Fig. 5G). In summary, ML2006a4 was as efficacious as NTV in promoting survival of mice infected with SARS-CoV-2 and provided superior viral RNA suppression.

The ketoamide adduct has an expended residence time.

To accurately assess binding affinity of the tighter inhibitors, we used the Morrison equation to calculate the equilibrium inhibitory constant, K_i, as previously described for NTV (10). We find that the δ-lactam containing ketoamide compounds inhibit M^{pro} at 20- to 100-fold lower concentrations than NTV or ETV at 37 ºC. In particular, we measured K_i values of 0.26 nM for ML2006a4 versus 4.5 nM for NTV and ETV (Fig. 3C and fig. S13).

To understand the basis for the higher affinity of ML2006a4 relative to NTV, we measured inhibitor binding and dissociation kinetics (fig. S14 to S15). The measured rate constants independently confirm the picomolar K_i-values found in the equilibrium inhibition experiments (table S5). Ketoamide-based inhibitors exhibit slower unbinding kinetics than NTV, with the ML2006a4 adduct showing a half-life of >5 h compared to <2 min for NTV (table S5). Our results align with other findings of slow dissociation by ketoamides, e.g., BPV and TPV from HCV protease (81) and leritrelvir from SARS-CoV-2 M^{pro} (17).

To determine the effect of dissociation half-life on antiviral activity, we monitored recovery of SARS-CoV-2 replication in Vero E6-TMPRSS2 cells following transient inhibition by ML2006a4 or NTV (fig. S16). To initiate the recovery of virus replication and mimic the process of in vivo drug clearance, the inhibitors were removed from the cell-culture medium to allow M^{pro} activity to resume. In comparison to NTV, ML2006a4 showed significantly ($p < 0.0001$) less viral replication at 4 h post drug removal (fig. S16). This suggests that the antiviral pharmacodynamics of ML2006a4 may extend beyond the pharmacokinetic curve due to the long residence time of ML2006a4.

Preorganization of the inhibitor improves affinity and specificity.

To study the role of preorganization at P2 in inhibitor affinity and specificity, we synthesized ML1201 and ML1206m as analogs of ML1001 and ML1006m, respectively, with a flexible P2 leucine (Fig. 2A). Both showed higher IC_{50} values than the parental proline-containing compounds (Fig. 2C). Although a P2 Leu allows a H-bond between its backbone NH and the side-chain of M^{pro} Gln189 (see e.g. PDB 6LU7) (63), this additional H-bond apparently cannot compensate for the entropic penalty of binding the more flexible ML1201 and ML1206m. Thus, the preorganized proline backbone, also present in ML2006a4 and NTV, allows removal of a HBD to enhance permeability while also improving binding energy.

We assessed the specificity of ML2006a4 and other M^{pro} inhibitors versus human cathepsins, which are common targets for protease inhibitors with electrophilic warheads (82). Although BPV has an acceptable side effect profile despite sub-micromolar inhibition of Cat-K and Cat-S (83), broader inhibition of cathepsins present a potential safety concern. We tested for inhibition of four human cathepsins: Cat-B/K/L/S (fig. S17). Cat-S appears to be the most promiscuous, as all ketoamides, except ML1006d, inhibited Cat-S with $IC_{50} < 1.5$ μM. However, at physiologically relevant concentrations, ML2006a4 showed

minimal inhibition of Cat-B/K/L. ML1201 and ML1206m, which contain Leu at P2, showed broader inhibition across the cathepsins than ML1001 and ML1006m with the Pro-derived P2 ring, revealing that preorganization at P2 also serves as a specificity determinant.

Ketoamide-based inhibitors have reduced sensitivity to resistance-associated mutations.

The history of HIV, HCV, and influenza antivirals cautions that resistance is likely to arise (84). Although NTV mimics the substrate envelope in P1–P4 (85), it differs from natural substrates in lacking a P1' analogue or the ability to form a tetrahedral adduct. Several potential NTV escape mutants have already been identified (32–34). One concerning M^{pro} mutation is S144A, as it maintains substantial proteolytic activity (25, 31, 86), is positioned near the reactive C145, was expanded during propagation of CoVs in the presence of NTV (32–34), and has been observed in natural SARS-CoV-2 genomes (24, 25, 33). Indeed, we observed a 12-fold K_i increase for NTV, from 4.5 nM against wild-type (WT) M^{pro} to 55 nM against M^{pro} S144A (Fig. 6, A and B). Similarly, S144A increased K_i 9.3-fold for nitrile-based PTV (Fig. 6B), 5.9-fold for aldehyde-based GC376, and 4.6-fold for hydroxymethyl ketone-based PF-00835231 (87) (table S6). The non-covalent inhibitor ETV saw a 31-fold increase in K_i (Fig. 6B). In contrast, ML2006a4 remained potent against M^{pro} S144A (Fig. 6A) with only a 2.4-fold increase in K_i (Fig. 6B).

To understand the structural basis for the differential susceptibility of NTV and ketoamide-based inhibitors to S144A (table S6), we obtained crystals of M^{pro} S144A bound to NTV or ML1006a. However, these did not reveal any clear differences from WT M^{pro} adducts (fig. S18). In the absence of conformational changes in the static crystals, we hypothesize that the ML1006a hemithioketal adduct forms a stronger interaction with the perturbed oxyanion loop of M^{pro} S144A compared to the thioimidate adduct of NTV. In addition, the P1' extension may provide further binding redundancy to help maintain recognition of mutant M^{pro}.

Other reported NTV escape mutants include M^{pro} E166X (32–34) and A173V (32, 33, 36). Mutation of E166 is surprising, since this residue is strictly conserved across all CoVs (88) and is involved in M^{pro} dimerization (89, 90). However, even if fitness loss is seen in single point mutants, several mutations outside the active site (e.g. T21I, L50F, P252L, and T304I) have been observed to restore viral fitness of a range of active site mutants including S144A and E166X (33, 34). Based on these findings, we also tested the effect of E166Q/A/V and A173V mutations on the M^{pro} affinities of NTV and ML2006a4 (Fig. 6B). Among these, L50F E166A, E166A, and E166V conferred the largest reductions in NTV affinity, and in all cases impacted ML2006a4 binding less. Specifically, the K_i of NTV versus ML2006a4 increased 26- versus 11-fold for L50F E166A, 43-versus 17-fold for E166A, and 2900-versus 430-fold for E166V (Fig. 6B and fig. S19). The other mutants tested, E166Q and A173V, conferred smaller and equal K_i increases for NTV and ML2006a4. In summary, ML2006a4 exhibits reduced sensitivity to the M^{pro} mutants that cause the largest loss of NTV binding.

We also tested the effects of the above mutations on binding of ETV and PTV, which differ from NTV and ML2006a4 in lacking BPV-derived moieties. First, ETV does not interact with the S4 pocket (fig. S20), making ETV insensitive to A173V that affects binding of NTV, ML2006a4, and, to a lesser extent, PTV (Fig. 6B). Compared to ML2006a4, the K_i values of ETV and PTV were less affected by E166V but more sensitive to E166A (Fig. 6B). In fact, E166V and E166A equally increased the K_i of ETV (68- and 56-fold) or PTV (36- and 30-fold). Both E166V and E166A may destabilize the dimer interface and the flexible S1 pocket (91), thereby affecting interactions with the M^{pro} inhibitors.

Next, we investigated potential mechanisms for sensitivity of NTV and ML2006a4 to E166V. Structural modelling indicates that E166V, but not E166A, can sterically clash with the P3 t-butyl of ML2006a4 and NTV (fig. S20), retained from BPV but absent in ETV and PTV. To test the role of the t-butyl, we synthesized ML2026a4 with a smaller isopropyl group in its place (Fig. 6C). As expected, ML2026a4 was less sensitive to E166V than ML2006a4, with a K_i increase of 67-fold versus 430-fold. The 67-fold reduced affinity of ML2026a4 against M^{pro} E166V was similar in magnitude to the 68-fold loss of affinity for ETV, which lacks a P3 group altogether.

Against WT M^{pro} and other mutants, the K_i of ML2026a4 was within 2-fold of ML2006a4, indicating that the P3 alteration in ML2026a4 does not substantially impact recognition of M^{pro}. In line with the K_i values, the antiviral EC_{50} values were only modestly higher for ML2026a4 than ML2006a4 (<3-fold) at 0.23 and 0.31 μM in Huh7.5.1++ and A549+, respectively (Fig. 6C). Thus, P3 branch reduction in ML2026a4 corrects the particular sensitivity of ML2006a4 to the E166V mutation, and may be a strategy for reducing the E166V-sensitivity of NTV and other BPV-derived M^{pro} inhibitors as well.

DISCUSSION

In this study, we develop ML2006a4 as a picomolar-affinity, orally dosable SARS-CoV-2 M^{pro} inhibitor with similar or superior antiviral efficacy to NTV at identical concentrations in vitro and identical doses in vivo. Overall, ML2006a4 and ML2026a4 are less sensitive to M^{pro} mutations compared to NTV and have mutational sensitivity profiles distinct from ETV. Our results identify ML2006a4 and ML2026a4 as potential preclinical drug candidates that can be developed to prepare for future surges of NTV- or ETV-resistant coronaviruses.

Interestingly, antiviral efficacy of the combination of NTV and RTV, the two ingredients in the Paxlovid oral COVID-19 treatment, had until recently not been reported in animals with initial reports focusing on high-dose (300 mg/kg) NTV alone (10, 92, 93). Recent studies tested the NTV+RTV combination for protection against severe disease at 150+10 mg/kg or 200+50 mg/kg in K18-hACE2 mice (19, 94, 95) and at 250+83 mg/kg in hamsters (96). Our results confirm that moderate doses of NTV+RTV (40+20 mg/kg), equivalent to the clinical doses in humans, do also efficiently rescue BALB/c mice from SARS-CoV-2-induced death. With this model in hand, we were able to compare ML2006a4 and NTV at identical doses, in identical vehicles, and with identical amounts of RTV, in parallel experiments. The comparison revealed that ML2006a4 was superior to NTV in reducing viral RNA copies in

mice. In addition, we found that therapeutic plasma concentrations of NTV or ML2006a4 could also be achieved without ritonavir by administering higher oral doses (Fig. 4C and 5A).

In the course of developing ML2006a4, we demonstrated that a P2 proline ring is essential for its potency. Multiple clinically approved protease inhibitors incorporate cyclic structures that improve affinity by preorganizing the molecules for binding (97, 98). In energetic terms, this is considered pre-paying the entropic penalty of binding-induced rigidification (99–101). Additionally, preorganization can improve selectivity and stability by limiting alternative conformations and disfavoring non-specific interactions (99, 100). Here, we directly compare inhibitors with flexible leucine or fixed proline P2 backbones, allowing us to identify the P2 proline as a major contributor to affinity, permeability, and specificity in ML2006a4 and NTV.

Another major outcome of this work is the development of a ketoamide warhead with improved lipophilicity and oral bioavailability. Specifically, the azetidine substitution introduced here solves the permeability limitations of earlier ketoamide-based SARS-CoV-2 M^{pro} inhibitors. Although azetidines are known motifs in drugs (102), the electrophilic azetidinylated α-ketoamide is an underexplored motif. To our knowledge, only three limited literature reports on the plain azetidinyl exist (53–55). Our demonstration of enhanced permeability and pharmacokinetics by azetidinyl derivatives should help expand the medicinal utility of ketoamides in covalent drugs.

Our study also reveals notable differences between ketoamide and nitrile warheads. First, ketoamides exhibit much slower bidirectional inhibition kinetics with dissociation half-lives of 5 h for ML2006a4 and 16 h for ML2006a2, and prolonged antiviral effects in cell culture. It would be interesting to determine if adduct stability could extend the pharmacodynamic profile and contribute to improved dosing protocols (81, 103). Second, the azetidinyl substitution provides a rigid platform for combined transition state or intermediate mimicry and interaction with S1’. In contrast, the nitrile warhead does not allow for extension or tuning.

Finally, ML2006a4 and ML2026a4 retained high potency against several M^{pro} mutants containing resistance-associated mutations of NTV or ETV. We speculate that the more extensive interactions of the ketoamide adduct or the azetidinyl group may provide a degree of redundancy in binding that is absent in NTV. The possibility of NTV resistance arising is especially concerning given the routine occurrence of rebound cases after NTV treatment (104, 105) and prolonged treatments of immunocompromised patients (48, 49), as these persistent infections provide favorable conditions for mutations to arise.

Our study has limitations. The profiling of resistance-associated mutants was only performed with purified M^{pro}-coil. Future work should focus on cross-resistance in the context of viral replication by measuring potency of ML2006a4 on SARS-CoV-2 replicons and recombinant viruses with NTV- or ETV-resistant mutations (33, 34). Furthermore, pharmacokinetics and in-vivo efficacy experiments were solely performed in mice. To improve preclinical predictions of efficacious human dosing, ML2006a4 pharmacokinetics

and pharmacodynamics should be determined in additional animal models following multiple dosing regiments.

In conclusion, we report the rational development of ML2006a4 as an oral picomolar-affinity SARS-CoV-2 M^{pro} inhibitor. Our design centered around a preorganized P2 bicyclic proline derivative, which we show improves affinity, permeability, and specificity. Azetidinyl derivatives of the ketoamide remove H-bond donors and improves membrane permeability and oral bioavailability, which is otherwise a key challenge for this potent but polar class of warheads. Similar to NTV, RTV-boosted ML2006a4 has high oral bioavailability in mice, and therapeutic oral administration rescued mice from an otherwise lethal SARS-CoV-2 infection. Importantly, the activity of ML2006a4 against M^{pro} was less sensitive to several resistance-associated mutations found for NTV or ETV, serving as an example of anticipatory drug design to address potential resistance mutants. Finally, the ketoamide derivative reported here may find broad use in smallmolecule inhibitors of other disease-relevant proteases.

MATERIALS AND METHODS

Study design

The study was designed to allow direct comparison of our lead compounds against NTV in vitro and the Paxlovid (NTV+RTV) dosing regime in vivo. The in vitro assays focused on binding affinity, residence time, cell permeability, antiviral potency in cell culture systems, and ADME profiling. The mouse experiments focused on pharmacokinetics and antiviral efficacy. The antiviral efficacy experiments were performed in mice using a human equivalent dose of NTV+RTV as the reference point.

Biosafety and animal handling

Infections, plaque assays, and fluorescence/luminescence readings of SARS-CoV-2 infected cell cultures occurred inside Class II biosafety cabinets under Biosafety Level 3 containment at Stanford University. The antiviral mouse efficacy experiments were performed under BSL3 containment at Galveston National Laboratory at University of Texas Medical Branch (UTMB) based on a protocol (2205027) approved by the Institutional Animal Care and Use Committee at UTMB. Mouse pharmacokinetics and tolerability studies were performed at the contract research organization Shanghai Chempartner. The mice were randomly assigned in all experiments.

Statistics

For details on statistical analyses, tests used, and replicates, see figure legends and Materials and Methods. Individual data for experiments where $n < 20$ are presented in data file S1.

Materials and Methods

The following reference compounds were purchased from commercial sources: boceprevir (BPV,Cayman Chemical, ≥ 98%), narlaprevir (NPV,AdooQ, ≥ 98%), telaprevir (TPV, AdooQ Bioscience, ≥ 98%), GC376 (AOBIOUS, ≥ 98%), ebselen (Cayman Chemical, ≥

99%), disulfiram (LKT Laboratories, ≥ 98%), ritonavir (RTV) for M^{pro} inhibition (Santa Cruz Biotechnology ≥ 98%) or ADME and PK (MedChemExpress and Selleckchem, ≥ 99.9%; or Macklin, 98.55%), Ensitrelvir fumarate (Medkoo, > 99%), PF-00835231 (Selleckchem, 99.08%), nirmatrelvir (NTV, Jinan Honest Pharm CO., > 99%)

Synthesis of ML inhibitors

ML1000 was synthesized by ACME Bioscience. All other ML-series compounds were synthesized by Shanghai Chempartner. NTV was initially synthesized on small scale by Shanghai Chempartner. The synthesis procedures are described in data file S2.

M^{pro} expression and purification

Modified versions of previous protocols based on human rhinovirus (HRV) 3C protease or SUMO protease (106) processing of severe acute respiratory syndrome coronavirus 2 (SARS-CoV-2) main protease (M^{pro}) fusion proteins were used to obtain purified M^{pro} with either native or extended termini after expression in E. coli. Specifically, SARS-CoV-2 M^{pro} variants were cloned as I) GST-M^{pro}-His_6, II) His_6-SUMO-M^{pro}, or III) His_6-SUMO-M^{pro}-coil fusions into a pET vector (Addgene plasmid #29666) using synthetic gene blocks for the M^{pro} portion of the SARS-CoV-2 polyprotein (pp1ab residue 3264–3569). M^{pro} point mutants were constructed in both constructs II and III. Constructs details are shown in fig. S21. In our hands, the His_6SUMO-M^{pro} fusions produced higher yields of soluble protein compared to the GST-M^{pro}-His_6 constructs. This is likely due to toxicity and growth retardation associated with M^{pro} activation upon autocatalytic removal of the GST-tag during expression of the GST-M^{pro}-His_6 fusion. In contrast, the His_6-SUMO-M^{pro} fusion is produced in full-length and only becomes fully active after SUMO-tag removal during subsequent purification steps.

SARS-CoV-2 M^{pro} expression plasmids were transformed into T7 Express lysY/I^q *E. coli* cells (New England Biolabs). Small overnight cultures in 2×YT media with 1% glycose were used to inoculate larger cultures in 2×YT media that were then grown at 37 °C to OD_{600} of about 0.8 before induction with 0.5 mM IPTG. After induction and 4–5 h growth at room temperature (RT, about 23 °C) the cells were harvested, and the pellets were frozen. Chemical lysis of the resuspended pellets was performed in B-PER (Thermo Scientific) supplemented with 40 U/mL Pierce universal nuclease (Thermo Scientific), and the supernatant cleared by centrifugation at 15000 g for 30 min. The soluble fraction was batch-absorbed onto INDIGO-Ni resin (Cube Biotech) in a buffer containing approximately a combined 45 mM Tris (pH ~7.8), 10 mM imidazole, 200 mM NaCl, and 2 mM DTT. The resin was loaded onto gravity flow columns and washed with 20 column volumes of wash buffer containing 50 mM Tris (pH 8.0), 25 mM imidazole, 300 mM NaCl, and 2 mM DTT. High purity protein was eluted in a buffer of 50 mM Tris (pH 8.0), 250 mM imidazole, 300 mM NaCl, and 2 mM DTT. Eluted fractions with high protein content were pooled and buffer exchanged into HRV protease cleavage buffer (50 mM Tris pH 7.3, 150 mM NaCl, 1 mM DTT) or SUMO protease cleavage buffer (50 mM Tris pH 8.0, 150 mM NaCl, 1 mM DTT). The proteins were cleaved by incubation with 1.5% (w/w) His-tagged HRV-3C

protease (Millipore Sigma SAE0045) or 10 U/mg His-tagged SUMO protease (Millipore Sigma SAE0067) by overnight incubation at 4 °C. The fully processed M^{pro} variants were then purified using reverse affinity chromatography to remove the His-tagged HRV and SUMO proteases and the cleaved His_6-tagged fusion-domains or peptides. Purity of the samples was checked on SDS-PAGE (>95%), and protein concentrations were determined based on A_{280} and predicted extinction coefficients.

Enzyme characterization

The proteolytic activity of purified M^{pro} was measured using Covidyte substrate peptides (AATBioquest) that incorporate either iFluor 670 (IF5) or Tide Fluor 5 (TF5) as a far-red fluorophore and Tide Quencher 5 (TQ5) as a quencher. Upon cleavage of IF5-VNSTLQ|SGLRK(TQ5)M (Covidyte IF670, fig. S2 and S3) or TF5-KTSAVLQ|SGFRKME(TQ5)M (Covidyte TF670, all other data) by M^{pro}, energy transfer to the quencher decreases and the fluorescence intensity increases. A Safire 2 microplate reader (TECAN) was used to monitor the fluorescence with excitation at 640/20 nm and emission at 680/20 nm. All measurements were performed as bottom-reads from lid- or film-covered 96-well plates (Greiner; μclear bottom medium binding or non-binding). The in vitro M^{pro} activity was measured in an assay buffer consisting of 50 mM Tris (pH 7.3), 50 mM NaCl, 1 mM EDTA, 3 mM DTT (fresh), 0.05% (v/v) TWEEN20 and 1% (v/v) DMSO. These conditions were used for all subsequent enzyme assays.

Michaelis-Menten parameters were obtained at 37 °C in the assay buffer. The same assay conditions were used to obtain the apparent equilibrium inhibition constants, $K_{i,app}$(see below). After 1 h of preheating of a well plate containing all solutions as 2× concentrated stocks, 45 μL of Covidyte TF670 substrate solution was transferred to 45 μL of protease solution and the fluorescence measurement immediately initiated on the microplate reader. The final concentration of protease was 50 nM, and the final concentration of substrate was 3–55 μM. The reaction was followed for 3–4 h at 37 °C. At the end of the measurement, the product formation had plateaued in all wells, and thus, all substrate molecules were assumed to have been consumed. Thus, to correct for inner filter effects, the end-point fluorescence signals were normalized to the known concentration of total substrate added to each well. The time-resolved product formation curves were fit (MathWorks MATLAB) with the full analytical solution to the differential equations of the Michaelis-Menten scheme (107):

$$[P(t)] = 1 - K_m \cdot W\left\{\frac{[S(0)]}{K_m} \cdot \exp\left(\frac{[S(0)] - k_{cat}[E]_T(t - t_0)}{K_m}\right)\right\} \quad \text{(Eq. 1)}$$

Here P is the product, S is the substrate, W is the Lambert W function, K_m is the substrate binding constant, k_{cat} is the zero-order rate constant of catalysis, $[E]_T$ is the total enzyme concentration, and t_0 accounts for a small delay in the first measurement after mixing the substrate and protease. During non-linear fitting, $[E]_T$ was fixed to 50 nM, [S(0)] was allowed to vary for the individual curves, and K_m, k_{cat} were globally optimized across the substrate dilution series. The results are presented in fig. S22. Michaelis-Menten parameters

could not be accurately determined for E166X mutants since the time-resolved product formation curves were not well-described by Eq. 1. Further investigations are required to fully understand the kinetics of M^{pro} E166X mediated proteolysis of Covidyte TF670.

In vitro M^{pro} inhibition assays – IC_{50}

For initial M^{pro} activity measurements, 150 nM M^{pro} was preincubated with varying concentrations of inhibitor for 30 min at 30 °C (Fig. S3) before adding IF670 substrate to a final concentration of 1.8 μM. The procedure was subsequently improved during the development of the M^{pro}-coil assay. For the data reported in Fig. 1 and 2, fig. S4, the following procedure was used: Following 15 min activation in assay buffer at RT, 1.5 nM M^{pro}-coil was preincubated in 60 μL assay buffer with varying concentrations of inhibitor in 96-well plates at RT for 1 h. Next, 30 μL TF670 substrate in assay buffer was added to a final concentration of 3 μM, and the measurement immediately initiated at 25 °C. In later assays, reported in Fig. 3 and 6, fig. S9, S13 and S19, the temperature during both preincubation and read-out was increased to 37 °C and the preincubation time was increased to 3 h to allow the slow-binding ketoamides to reach equilibrium with M^{pro}-coil (fig. S23). The other parameters were unchanged. When running the assay at 37 °C, the substrate solution was preheated before addition to the well plate.

The rate of substrate cleavage was extracted as the initial linear fluorescence increase and normalized against the rate of substrate cleavage in the absence of inhibitor, I, to obtain the relative activity,v_{rel}. From this, the 50% inhibitory concentration (IC_{50}) was obtained using a four-parameter logistic function (MathWorks MATLAB):

$$v_{\mathrm{rel}} = v_{\max} - \frac{(v_{max} - v_{min})}{1 + 1^{n_H(-pIC_{50} - \log([I]_T))}} \quad \text{(Eq. 2)}$$

The maximal and minimal rates of substrate cleavage, v_{max} and v_{min}, $pIC_{50} = -\log(IC_{50})$, and the Hill coefficient, n_H were all free fitting parameters in the non-linear fitting routine. The inhibitor concentration, $[I]_T$, is the total concentration of inhibitor during the preincubation.

Calculation of the thermodynamic inhibitory constant – K_i

The IC_{50} data presented in Fig. 3 and fig. S9 was further analyzed, as many of the inhibition curves showed the characteristics of tight binding $(IC_{50} \leq [M^{pro} - \mathrm{coil}])$. $K_{i,app}$ values were extracted by fitting (MathWorks MATLAB) the relative protease activity, v_{rel}, as a function of total inhibitor concentration, $[I]_T$, with the Morrison equation (108):

$$v_{rel} = v_{max} - (v_{max} - v_{min})\frac{([E]_T + [I]_T + K_{i,app}) - \sqrt{([E]_T + [I]_T + K_{i,app})^2 - 4[E]_T[I]_T}}{2[E]_T} \quad \text{(Eq. 3)}$$

Here, $[E]_T$, is the total concentration of active enzyme (active $\left[M^{pro} - coil\right]_T$), and $K_{i,app}$ is the apparent inhibition constant. Since M^{pro} is only active as a dimer and the exact fraction of active dimeric M^{pro}-coil is unknown, when working in the low nM range, $[E]_T$ was initially chosen to be a fitting parameter instead of fixed at 1.5 nM (the total concentration of M^{pro}-coil in solution). Specifically, $K_{i,app}$, v_{max}, and v_{min} were allowed to take individual values for each dataset, whereas $[E]_T$ was treated as a global parameter for all fits (fig. S13). The extracted concentrations of M^{pro} active sites were 1.5 nM for both wild-type (WT) and S144A, respectively, in agreement with the total concentration of 1.5 nM added M^{pro}-coil. This supports that the M^{pro}-coil proteins are present as active dimers even at low nM concentrations.

The datasets recorded for ML2006a titrated against both M^{pro}-coil WT and S144A were not well-described by Eq. 3 when using the M^{pro}-coil concentrations from the global fitting routine. The problem appears to arise from ML2006a being the tightest binding inhibitor, and even the high-quality data presented in fig. S13 did not have enough datapoints along the steep transition of the inhibition curve for this specific inhibitor. Thus, when fitting the data for ML2006a, $[E]_T$ was included as an individual fitting parameter without constraints from the global fit. From this procedure, $[E]_T$ was estimated to 1.1 nM and 1.0 nM for the WT and S144A M^{pro}-coil ML2006a datasets, respectively. These numbers are still in good agreement with the numbers reported above, but highlights the challenges in applying Eq. 3 when $K_{i,app} \ll [E]_T$ (108).

For all mutants, other than S144A, $[E]_T$ was fixed at the preincubation concentration of added M^{pro}-coil since these datasets did not contain enough datapoints in the tight binding limit to obtain stable estimates of $[E]_T$ from the global fitting routine. This procedure also resulted in good fits (fig. S19).

We assume that $K_i = K_{i,app}$ since 1) $[S] < < K_m$(e.g., $[S] = 3$ μM versus $K_m = 44$ μM for WT M^{pro}-coil, fig. S22) and 2) several of the tested inhibitors show slow dissociation kinetics which invalidates the Cheng-Prusoff correction. Specifically, the Cheng-Prusoff equation is derived based on the assumption that both the substrate and the inhibitor are in equilibrium with the enzyme during the assay (109). However, since the inhibitors are preincubated in the absence of substrate and only the initial rate of substrate proteolysis is used in our analysis, the inhibitors have not dissociated from active site and equilibrated with the substrate during fluorescence read-out. Effectively, we assume that the substrate does not compete with the M^{pro} inhibitors during the short measurement time of this assay.

Inhibitor binding kinetics

Inhibitor binding kinetics were investigated in a time-resolved association experiment at 37 °C. An inhibitor dilution series was prepared and premixed with Covidyte TF670 substrate in a 96-well plate. After preheating for 1 h at 37 °C, 60 μL of combined substrate and inhibitor premix was added to 30 μL of M^{pro} coil WT solution, and recording of the progress curves of substrate proteolysis was immediately initiated on the Safire 2 microplate

reader (TECAN) with excitation at 640/20 nm and emission at 680/20 nm. The final concentrations in the assay buffer were 6 μM of substrate, 1 nM of M^{pro}-coil WT, and inhibitor concentration as annotated in fig. S14. The kinetics were monitored for 1 h, and the progression curves for each inhibitor were globally fit (MathWorks MATLAB) to a simple two-state reversible binding model (108):

$$I_t = v_s(t - t_0) + \frac{(v_i - v_s)}{k_{off} + k_{on,app}[1]_T}(1 - \exp\{-(k_{off} + k_{on,app}[I]_T)(t - t_0)\}) \quad \text{(Eq. 4)}$$

Here, v_i and v_s are the relative initial and steady-state rates of product formation, $k_{on,app}$ and k_{off} are the first and zero order rate constants of a 2-state binding model ($E + I \leftrightharpoons EI$), and t_0 is included to account for the small time-delay of measurement initiation. During non-linear regression of each inhibitor dataset (fig. S14), v_i, $k_{on,app}$, k_{off}, and t_0 were treated as global fitting parameters, whereas v_s is a free fitting parameter at each concentration. The substrate independent association constant, k_{on}, was calculated as $k_{on,app} \cdot (1 + [S]/K_m)$ to correct for the direct competition for M^{pro} binding between the substrate and the inhibitor that are added simultaneously in this experiment (108) (table S5). Using this method, the data was sufficiently described by the two-state binding model. More complicated binding models (e.g., preequilibrium induced fit) were also explored and cannot be ruled out based on current data. For example, an induced fit model with a very weak encounter complex ($K_{i,encounter} > > K_i$) was fully consistent with the data (108). However, the more advanced models did not improve the fit quality. The binding kinetics of NTV were too fast for quantification at 37 °C. Thus, the experiment described above was also performed for NTV at 25 °C. The substrate concentration was 3 μM in this experiment, and all other conditions identical to the assay at 37 °C.

Inhibitor dissociation kinetics

Dissociation kinetics were measured for select inhibitors using recovery of proteolytic activity following dilution of preformed M^{pro}-coil inhibitor adducts. The adduct was formed by incubating 2 μM M^{pro}-coil with 3 μM inhibitor for 1 h at 37 °C in assay buffer. The adduct was quickly diluted 1000-fold into the assay buffer containing Covidyte TF670 substrate in a 96-well plate. The dilution was performed in two steps: 1) 5 μL of adduct was mixed with 195 μL assay buffer, 2) 5 μL of solution from step 1 was mixed with 120 μL of substrate-containing assay buffer. The final assay solutions contained 2 nM M^{pro}-coil, 3 nM inhibitor, and 26 or 52 μM Covidyte TF670 substrate. The fluorescence intensities were monitored for 5 h at 37 °C using the Safire 2 microplate reader (TECAN) with excitation at 640/20 nm and emission at 680/20 nm. In a procedure identical to the calibration that was performed in the enzyme characterization assay, the recorded fluorescence intensities were background corrected and transformed into product concentrations using control wells that contained fully cleaved substrate.

The resulting data were fit using a numerical global differential equation solver (KinTek Explorer 11, KinTek) (110). The differential equations were generated based on the following reaction mechanism:

$$E + S \leftrightharpoons ES \rightarrow E + P\{k_1, k_{-1}, k_{cat}\}$$
$$E + I \leftrightharpoons EI\{k_{on}, k_{off}\}$$

Here, k_1, k_{-1}, and k_{cat} are the reaction rates associated with catalytic substrate turnover by WT M^{pro}-coil, and k_{on} and k_{off} are the binding and dissociation rates of the inhibitor binding to WT M^{pro}-coil. For each inhibitor, the independently measured k_{on} (fig. S14 and table S5) was fixed during fitting. The Michaelis Menten parameters ($K_m = (k_{k-1} + k_{cat})/k_1 = 44\ \mu M^{-1}S^{-1}$ and $k_{cat} = 2\ s^{-1}$) had been determined in independent experiments. The value of k_{cat} was kept fixed during data fitting. Next, we assume that the binding rate of the substrate is substantially faster than the binding rate of the slow ketoamide-based inhibitors. Thus, assuming $k_1 > 1\ \mu M^{-1}S^{-1}$ and using the values of K_m and k_{cat}, it follows that $k_{-1} >> k_{cat}$. In this pre-equilibrium limit, the k_{off} value that is retrieved from the fits, is independent of the absolute values of k_1 and k_{-1} since $K_m \sim k_{-1}/k_1$ in this limit. We thus fixed k_1 to 10 $\mu M^{-1}S^{-1}$ and k_{-1} to 438 s^{-1} during fitting. Finally, the fitting routine was allowed to correct for minor variance in the substrate concentrations and baseline values at t = 0. The resulting fits and k_{off} values are presented in fig. S15 and table S5.

Cathepsin inhibition assays

Recombinant human cathepsins, Cat-B (R&D Systems, 953-CY), Cat-K (EMD Millipore, 219461), Cat-L (R&D Systems, 953-CY), or Cat-S (Sino Biological, 10487-H08H), were first activated for 15 min in 50 mM MES pH 5.5, 1 mM EDTA, 6 mM DTT. Next, inhibitors were added to concentrations of 15 μM or 1.5 μM and incubated with the protease (75/15/15/150 pg/mL Cat-B/K/L/S) in 60 μL 50 mM MES pH 5.5, 1 mM EDTA, 3 mM DTT, 0.5% DMSO for 1 h at RT in 96-well plates (Greiner; μclear bottom nonbinding). After addition of 30 μL fluorogenic Z-LR-AMC substrate peptide (R&D Systems) to a final concentration of 20 μM, the reaction was immediately followed at RT using the Safire 2 microplate reader (TECAN) with excitation at 380/20 nm and emission detection at 460/20 nm. The initial substrate cleavage rate was determined by fitting a linear function to fluorescence signal. The remaining activity was obtained as the substrate cleavage rate relative to a 0.5% DMSO-only control.

Crystallography

Mature SARS-CoV-2 M^{pro} was buffer exchanged into a solution of 20 mM Tris pH 7.3, 2 mM DTT or 3 mM TCEP using Amicon Ultra-4 10K centrifugal filters (Millipore). Immediately after buffer exchange, M^{pro} was incubated with inhibitor for a minimum of 1 h at RT before dispensing sitting drops on Intelliplates 96–3 LVR (Hampton Research) using a Oryx8 crystallization robot (Douglas Instruments). The plates were incubated at 16 °C. Crystals formed under a range of conditions (table S7) from either commercial screens or from custom optimization screens that were prepared with a Scorpion Screen Builder (Art

Robbins Instruments). Crystals were harvested and added to precipitant solution mixed with cryoprotectant and cryocooled by plunging into liquid N_2.

In general, crystals from a single crystallization condition showed a wide variation in X-ray diffracting power, and therefore a large number of crystals were screened for initial data quality assessment. The best candidates were selected and stored for further data collection. In some cases, X-ray diffracting raster sampling was combined with microfocus (15 × 15 μm) to find the best diffracting region on the crystal, or alternatively microfocus was combined with helical data collection by sliding along the longest axis of the crystal. Data collections were performed at 100 K using Stanford Synchrotron Radiation Lightsource (SSRL) beamlines BL12–1 and BL12–2 (SLAC National Accelerator Laboratory) (111).

Data were reduced with XDS (112) or DIALS (113), scaled with SCALA (114) or AIMLESS (115), and analyzed with different computing modules within the CCP4 suite (116) or CCP4i2 suite (117). Crystals belonged to the orthorhombic $P2_12_12$ or monoclinic C2 space groups and contained one polypeptide chain per asymmetry unit (table S8). Structures were solved by the molecular replacement method with Phaser (118) using the polypeptide chain of SARS-CoV-2 M^{pro} of PDB 6LZE (60) as the search model. Refinement was performed using REFMAC (119) with manual refinement performed in COOT (120).

Cell-based M^{pro} activity assays

HEK293A cells (ATCC) were cultured at 37 ºC in 5% CO_2 in Dulbecco's Modified Eagle's Medium (DMEM, Gibco 31053036) supplemented with 10% fetal bovine serum (FBS) (GeminiBio) and 100 U/mL penicillin + 100 μg/mL streptomycin (GeminiBio). Huh7 cells (ATCC) were cultured at 37 ºC in 5% CO_2 in Roswell Park Memorial Institute 1640 medium (RPMI-1640, Life Technologies) supplemented with 10% FBS and 100 U/mL penicillin + 100 μg/mL streptomycin.

The M^{pro} activity assay in HEK293A was performed by using western blotting to monitor substrate proteolysis. Cells were transfected with 100 ng of a pcDNA3.1/Puro-CAG plasmid containing the construct shown in fig. S2A using Lipofectamine 3000 (Invitrogen) in Opti-MEM (Life Technologies) according to the manufacturer's protocol. TPV and BPV were added 2 h post-transfection. 24 h post-transfection, cells were washed twice with phosphate buffered saline (PBS), then lysed with 50 μL of 50% 4× LDS sample buffer (NuPAGE, Life Technologies) and 10% 2-mercaptoethanol, and DNA was sheared by sonication. After heating at 80–90 °C for 1–2 min, cell lysates were loaded onto 4–12% Bis-Tris gels (NuPAGE, Life Technologies) along with a Precision Plus protein dual-color standard (Bio-Rad). Protein bands were transferred to polyvinylidene fluoride membranes using a Trans-Blot Turbo Transfer System (Bio-Rad) and blocked with SuperBlock T20 (TBS) blocking buffer (Thermo Scientific). Membranes were probed with primary antibodies in SuperBlock T20 (TBS) blocking buffer and fluorophore-conjugated secondary antibodies in SuperBlock (TBS) blocking buffer (Thermo Scientific), with 3 washes in SuperBlock T20 (TBS) blocking buffer after each step. Membranes were imaged using an Odyssey imaging system (LI-COR) and signals quantified using ImageJ. The following primary antibodies were used for immunoblotting at the indicated dilutions: mouse monoclonal anti-FLAG

(Sigma-Aldrich, F1804), 1:2000; rabbit polyclonal anti-beta actin (Abcam, ab8227), 1:5000. Secondary antibodies were IRDye 680RD goat-anti-rabbit (LI-COR, 926–68071) and IRDye 800CW goat-anti-mouse (LI-COR, 926–32210), used at 1:5000 dilution each.

We developed a M^{pro} activity assay in Huh7 cells based on proteolysis of a NanoBiT luciferase reporter. A schematic of this assay is presented in fig. S24. Huh7 cells were seeded as 10000 cells/well into solid white Lumitrac 96-well microplates (Greiner). 24 h later, cells were transfected with 10 ng reporter plasmid with 40 ng carrier DNA plasmid (pcDNA3.1 vector) using Lipofectamine 3000, following manufacturer's instructions. 24 h post-transfection, inhibitor dilutions in DMSO (final concentration < 0.33%) were added to the cell culture. 48 h post-transfection, cells were lysed, and Nano-Glo Luciferase Assay System (Promega) added according to the manufacturer's instructions. After mixing the assay solution thoroughly, the luminescence signal was read using the Safire 2 microplate reader (TECAN) with an integration time of 1000 ms and a speed of 1 read/min. The maximum signal within the first 15 min was used for data analysis. The data was normalized against a DMSO control (low luminescence) and a full inhibition control (high luminescence) to obtain the relative luminescence intensity, I_{rel}, that correlates with intracellular M^{pro} activity. The data was fit to Eq. 5 (MathWorks MATLAB) to obtain $IC_{50,cell}$:

$$I_{\mathrm{rel}} = I_{\min} + \frac{(I_{max} - I_{min})}{1 + 10^{n_H(-pIC_{50,\mathrm{cell}} - \log([I]_T))}} \quad \text{(Eq. 5)}$$

Antiviral assays with SARS-CoV-2-nLuc in A549-ACE2 and Huh7.5.1-ACE2-TMPRSS2

A549-ACE2 (A549+) and Huh7.5.1-ACE2-TMPRSS2 (Huh7.5.1++) cells (121, 122) were maintained in D10 growth media (DMEM, Gibco 11885084) supplemented with 10% FBS (GeminiBio), 2 mM L-glutamine, 10 mM HEPES, 1 mM sodium pyruvate, 1% non-essential amino acids, and 1% antibioticantimycotic (all supplements from Gibco)). In addition, the media was supplemented with 0.5 mg/mL geneticin (Gibco) and 0.2 mg/mL hygromycin (Gibco) for A549+ or Huh7.5.1++, respectively. SARS-CoV-2-nLuc (USA-WA1/2020 strain expressing nLuc) virus (123) was passaged twice in Vero E6 cells (ATCC) and titered by plaque assay on Vero E6 cells and confirmed by deep sequencing. The antiviral replication assay was performed in D2 assay media (D10 media adjusted to 2% FBS and without antibiotics).

Inhibitors were added in D2 media to A549+ or Huh7.5.1++ cells 24 h after plating the cells in solid white 96-well plates. Control wells were treated with equal concentrations of DMSO. Within 15 min of drug addition, cells were infected with virus at an MOI of 0.1. After 2 h, the cells were washed with PBS, and followingly incubated with drug for 48 h postinfection (hpi) before addition of lytic Nano-Glo assay (Promega) and reading on a GloMax Discovery plate reader (Promega). The plates always contained a positive inhibition control (e.g., GC376 or NTV), a DMSO control column as positive infection control, and a column without cells for background signal subtraction. The 10-base logarithm of the luminescent signal was background-corrected and normalized against the DMSO control to represent the relative viral replication rate. The 50% effective antiviral concentration

(EC_{50}) was obtained by fitting the relative viral replication rate as a function of the inhibitor concentration to Eq. 2 (MathWorks MATLAB) with IC_{50} replaced by EC_{50}.

Antiviral effect in Calu-3 cells

Calu-3 cells (human lung epithelium, ATCC) were cultured at 37 ºC in 5% CO_2 in DMEM (Gibco) supplemented with 10% fetal calf serum (FCS; Omega Scientific Inc.), 1% penicillin/streptomycin (Gibco) and 1% nonessential amino acids (Gibco). Vero E6 cells were cultured at 37 ºC in 5% CO_2 in DMEM (Corning) supplemented with 10% FBS (Omega Scientific), 2 mM L-glutamine, 1% penicillin/streptomycin, 1% nonessential amino acids, 1% HEPES, and 1% Sodium pyruvate (all Gibco).

Calu-3 were pretreated with M^{pro} inhibitors and infected with SARS-CoV-2 (USA-WA1/2020) (124) at a multiplicity of infection (MOI) of 0.1 in DMEM containing 2% FCS. After 1 h incubation at 37 °C, the viral inoculum was removed, cells were washed and supplemented with fresh medium containing inhibitors. Culture supernatants were harvested at 24 hpi and the viral titers were measured by plaque assays.

For plaque assays, monolayers of Vero E6 cells were infected with supernatants from Calu-3 cultures for 1 h at 37 °C. Cells were then overlaid with Eagle's Minimum Essential Medium (EMEM) 2X without Phenol Red and L-Glu (Quality Biological) and carboxymethyl cellulose and incubated at 37 °C. At 72 hpi, the overlay was removed, and the cells were submerged in 70% ethanol for fixation and viral inactivation followed by crystal violet staining. Viral titers (PFU/mL inoculum) were quantified according to standard methods (125) and normalized against a DMSO-only control group. EC_{50} values were obtained by fitting (Prism 9, GraphPad) the relative viral titers to Eq. 2 with v_{min} and v_{max} set to 0% and 100%, respectively and IC_{50} replaced by EC_{50}.

Antiviral assays with drug washout in Vero E6-TMPRSS2 cells

Vero E6-TMPRSS2 cells (JCRB1819, XenoTech) were cultured at 37 ºC in 5% CO_2 in DMEM (Gibco) supplemented with 10% FBS (Omega Scientific), 1% penicillin/streptomycin (Gibco), and 1 mg/mL G418 (Gibco). Vero E6-TMPRSS2 cells were inoculated with SARS-CoV-2-nLuc (USA-WA1/2020) (124) at an MOI of 1 in DMEM containing 2% FBS at 4°C for 1 h to synchronize virus attachment. Next, the cells were incubated at 37 °C for 1 h to allow virus entry, followed by virus inoculum removal and twice repeated washing with PBS. NTV, ML2006a2, or ML2006a4 were then added to the cells at 10 or 30 μM. After 6 h of incubation with inhibitor (7 hpi), the supernatants were removed, and cells were washed twice with PBS. Fresh medium was then added, and the cells incubated for another 4 h until 11 hpi. At 7 and 11 hpi, the amounts of virus replication were determined by nLuc expression using the lytic Nano-Glo assay (Promega) and reading on a GloMax Discovery plate reader (Promega) with 0.3 s integration time. Background correction was performed using non-infected cells. Statistical analysis of the replication values was performed in Prism 9 (GraphPad) as an ordinary one-way analysis of variance (ANOVA) with a post-hoc Tukey correction for multiple comparisons between all groups. The adjusted p-values are presented in fig. S16 together with the relevant data.

Cytotoxicity assays in Huh7, A549-ACE2, and SARS-CoV-2 infected Calu-3 cells

24 h prior to the inhibitor treatment, 10000 Huh7 cells (RPMI with 10% FBS, 100 U/mL penicillin + 100 μg/mL streptomycin) or A549+ cells (D10 media) were seeded in 100 μL culture medium in solid white 96-well plates. The next day, the culture medium was replaced with fresh media containing inhibitors at the desired concentration (1–100 μM). Staurosporine (0.1 μM or 1 μM), a non-selective protein kinase inhibitor known to induce apoptosis, was used as a positive control. After 72 h, cell viability was determined using the CellTiter-Glo 2.0 kit (Promega) according to the instructions of the manufacturer. The luminescence signal was measured on the Safire 2 microplate reader (TECAN) with 1 s integration time. Cell viability was also assessed in Calu-3 cells infected with SARS-CoV-2 using alamarBlue (Invitrogen) according to the manufacturer's protocol. Fluorescence was detected with excitation at 520 nm and emission at 580−640 nm on a GloMax Discover microplate reader (Promega).

ADME

All in vitro ADME experiments were performed at Shanghai Chempartner. All concentration measurements were performed by LC-MS/MS. The apparent permeability, P_{app}, was measured as diffusion of 10 μM compound across Caco-2 cell layers in both the apical-to-basal (A-B) and the basal-to-apical (B-A) direction over a period of 90 min. The assay was performed in Hanks' Balanced Salt solution (HBSS) at 37 °C. Quality control was performed using the following reference compounds: erythromycin, metoprolol, atenolol, and lucifer yellow. To improve comparison of P_{app} measured in independent assays, P_{app} was normalized to both erythromycin and atenolol in each assay, and the absolute mean P_{app} calculated after multiplying the following mean values obtained for the reference compounds (in units of 10^{-6} cm/s ± SD): atenolol: $P_{app,A\text{-}B} 0.53 \pm 0.34, P_{app,B\text{-}A} = 0.73 \pm 0.38$; erythromycin: $P_{app,A\text{-}B} = 0.25 \pm 0.20, P_{app,B-A} = 18.6 \pm 4.6$.

Kinetic solubility was measured after adding compound to a final concentration of 100 μM in PBS (pH 7.4, 1% DMSO) and incubating with shaking for 1 h at RT. Precipitate was spun down before measuring the dissolved concentration. Propranolol, ketoconazole, and tamoxifen served as controls.

Plasma protein binding was measured in either 100% or 10% C57BL/6 mouse plasma or 100% human plasma after dialysis at 37 °C for 5 h. Plasma was diluted in in 0.05 mM sodium phosphate buffer (pH 7.4). The initial compound concentration was 1 μM (0.2% DMSO). Warfarin and Quinidine served as reference compounds. The samples were quenched with MeCN. The recovered fraction was > 70% in all cases, except for ML2006a4 (46% in 10% mouse plasma and 68% in 100% human plasma). The reduced recovery for ML2006a4 is not expected to affect the accuracy of the results (126). From measurements in 10% plasma, the fraction of unbound compound, $f_{u,p}$, at 100% plasma concentration was extrapolated using the method described by Di et al. (127).

Plasma stability at 37 °C was measured in a solution consisting of 90% CD-1 mouse or human plasma and 10% 0.05 mM sodium phosphate buffer (pH 7.4) containing 0.5% bovine serum albumin. The starting concentration of the compounds were 2 μM (0.4% DMSO), and

samples were collected and quenched with MeCN at 0, 5, 15, 30, 45, and 60 min. Linear regression of ln([compound]) versus time was used to determine the half-life,$t_{1/2,p}$. Procaine was used to check plasma activity.

Microsomal metabolic stability of the compounds was measured in 0.5 mg/mL CD-1 mouse (Corning or Xenotech) or human liver microsomes (Corning) for 45 min at 37 °C in 0.1 M potassium phosphate buffer (pH 7.4) with 1.0 mM EDTA. The starting concentration of the compounds was 1 μM (0.1% MeCN). For a second set of measurements, 1 μM RTV was added as a CYP3A inhibitor (128). The reactions were initiated by the addition of 6 mM NADPH, and samples were quenched with MeCN at 0, 5, 14, 30, 45 min. Linear regression of ln([compound]) versus time was used to determine the half-life, $t_{1/2}$, and the related apparent intrinsic clearance: $CL_{int,app} = \ln(2)/(t_{1/2} \cdot C_{microsome})$. Testosterone was used for quality control.

Pharmacokinetics using a saline PEG300/DMSO/Tween-80 (PDT) formulation

Single dose pharmacokinetic studies were performed at Shanghai Chempartner for ML1006m, ML1006a, ML2006a, ML2006a4, NTV, and PTV in male 6- to 8-week-old non-fasted C57BL/6 mice. Each measurement series consisted of 9 mice and 9 time points (pre-dose, 0.08, 0.25, 0.5, 1, 2, 4, 8, and 24 h). The mice were sampled in groups of 3, and each mouse was used for sparse sampling at three interspersed time points ($n = 3/timepoint$). At each timepoint, about 110 μL blood was collected into K_2EDTA tubes through facial vein bleeding. Plasma samples were put on ice and centrifuged to obtain plasma sample (2000 g for 5 min at 4 ℃) within 15 min of collection. The plasma samples were stored at −70 ℃ until analysis. At the terminal point of each series (4, 8, or 24 h) both lungs were collected from all mice. No abnormal clinical signs were observed during the studies. The lung samples were homogenized with 3 volumes (v/w) of PBS. Compound concentrations in plasma and lungs were quantified at the end of the experiment using LC-MS/MS detection. The PK parameters were calculated from the mean plasma concentration of the pooled data of each group ($n = 3$) versus time using a non-compartmental analysis implemented in the PKSolver software with linear trapezoidal integration (129). Parameter uncertainty estimates were obtained by performing two additional non-compartmental analyses on the mean plasma concentration ± SD, respectively.

All compounds were formulated as colorless clear solutions in 45% saline, 40% PEG300, 10% DMSO, 5% Tween-80 (PDT). Four groups were tested. In group 1, oral doses (po, 20 mg/kg at 10 mL/kg) were administered, whereas in group 2, intravenous doses (iv, 2.0 mg/kg at 5 mL/kg) were administered. In groups 3 and 4, oral dosing of RTV (po, 20 mg/kg at 10 mL/kg) was performed 30 min before po or iv dosing of M^{pro} inhibitors at the same doses as group 1 and 2, respectively. The RTV dose was set based on allometric scaling of a typical human PK enhancing RTV dose of 100 mg (130). Thus, for a human dose of 1.7 mg/kg (assuming mean body mass of 60 kg) the equivalent dose in mice is about 20 mg/kg based on a allometric scaling factor of 12.3 (131).

Pharmacokinetics and tolerability assessment using a methylcellulose/Tween-80 formulation

At Shanghai Chempartner, ML2006a4 and NTV were formulated together with RTV as co-suspensions in 0.5% methylcellulose and 2% Tween-80 in water (MCT-2). Plasma concentrations were monitored after oral administration of single doses of ML2006a4+RTV or NTV+RTV (po, 20+20 mg/kg at 5 mL/kg or 40+20 mg/kg at 10 mL/kg) in 6- to 8-week-old male C57BL/6 mice ($n = 3/timepoint$). The study was performed as described for the PDT formulation, except lungs were not collected.

For the dose tolerability study, four groups of 8- to 12-week-old female C57BL/6 mice ($n = 6$) received oral dosing at 10 mL/kg twice daily for 4 days. The four groups were 1) vehicle-only control, 2) RTV (20 mg/kg), 3) ML2006a4+RTV (40+20 mg/kg), and 4) NTV+RTV (40+20 mg/kg). The mice were observed twice daily and weighed once daily. No clinical abnormalities were registered. At the end of the study, blood was collected 12 h after administration of the final dose and used to run standard hematology and clinical chemistry panels (table S3 and S4).

Pharmacokinetics of high-dose single-agent ML2006a4 and NTV

At Shanghai Chempartner, ML2006a4 and NTV were formulated as suspensions in 0.5% methylcellulose and 5% Tween-80 in water (MCT-5). Plasma concentrations were monitored after oral administration of single doses of ML2006a4 or NTV (po, 300 mg/kg at 10 mL/kg) in 6- to 8-week-old male C57BL/6 mice. Each measurement series consisted of 6 mice and 6 time points (0.5, 1, 2, 4, 8, and 12 h). The mice were sampled in groups of 3, and each mouse was used for sparse sampling at three interspersed time points ($n = 3/timepoint$). Otherwise, the study was performed as described above but without lung collection.

Antiviral efficacy in mice

The antiviral efficacy experiments were performed under BSL3 containment at Galveston National Laboratory at University of Texas Medical Branch at Galveston, Texas (UTMB). Mouse adapted SARS-CoV-2 MA10 was propagated and titered in Vero E6 cells. Vero E6 cells (ATCC, CRL:1586) were grown in Minimum Essential Medium (MEM, Gibco) supplemented with penicillin (100 units/mL), streptomycin (100 μg/mL) and 10% FBS. The SARS-CoV-2 MA10 was stored in MEM supplemented with 2% FBS at −80 °C until needed.

A total of 40 female BALB/c mice aged 15 to 16 weeks (Jackson Laboratory, 000651) were randomly separated into 5 groups for the study. Groups 1) RTV (20 mg/kg), 2) NTV+RTV (40+20 mg/kg), 3) ML2006a4+RTV (40+20 mg/kg) ($N = 10$) were anesthetized with isoflurane and challenged with 10^5 $TCID_{50}$/60 μL (50% tissue culture infectious dose in 60 μL) of SARS-CoV-2 MA10 (132) through the intranasal route. Mice of group 4) NTV+RTV (40+20 mg/kg) and 5) ML2006a4+RTV (40+20 mg/kg) ($N = 5$) were not challenged with virus and served as control groups to test the tolerability of the indicated test articles. Starting 2 h post infection, mice were treated orally with the indicated test articles at 10 mL/kg twice daily for 4 days. Mice were weighed daily and, at least once daily, clinically observed and scored based on a 1–4 grading system (1: Healthy, 2: ruffled fur,

lethargic, 3: hunched posture, orbital tightening, increased respiratory rate, > 15% weight loss, and 4: dyspnea, cyanosis, reluctance to move when stimulated, > 20% weight loss). Mice with a clinical score of 4 were immediately euthanized and their lungs collected. Otherwise, five mice in group 1, 2 and 3 were euthanized as planned at 2 dpi, and their lungs were collected for viral load quantification and histopathology assessments. Observation of the remaining five mice per group continued for up to 6 dpi before euthanasia and immediate lung collection. First, lungs were inflated and rinsed with PBS. Then, the inferior and post-caval lobes of the right lung were collected and frozen for infectious viral load quantification. Next, the superior and middle lobes of the right lung were collected and stored in RNAlater (Invitrogen) for quantification of viral RNA loads. Finally, the left lung was fixed in 10% buffered formalin in preparation for histology assessments.

For quantitation of viral titers in the lung tissue, the frozen lung specimens were weighed before homogenization in PBS/2% FBS solution using a TissueLyser (Qiagen), as previously described (133). After centrifugation at 3000 g, supernatants were used to quantify infectious virus titers in a standard Vero E6 cell-based infectivity assays in 96-well plates (134). Viral titers were expressed as 50% tissue culture infectious dose per gram of tissue ($TCID_{50}$/g). Statistical analysis of virus titers was performed in Prism 9 (GraphPad) as an ordinary one-way analysis of variance (ANOVA) with a post-hoc Tukey correction for multiple comparisons between all groups ($n = 5/timepoint$). The adjusted p-values are presented in Fig. 4F together with the relevant data.

For RNA extraction and quantitative RT-PCR, lung tissues were weighed and homogenized in 1 mL of Trizol reagent (Invitrogen) using TissueLyser (Qiagen). The RNA was then extracted using Directzol RNA miniprep kits (Zymo research) according to the manufacturer's instructions. To quantify the viral copies, RNA was reverse transcribed using iScript cDNA Synthesis kits (Bio-Rad, 1708891) according to the manufacturer's instructions. The cDNA was then amplified using iQ SYBR green supermix (Bio-Rad) and a CFX96 real-time PCR detection system (Bio-Rad). Primer sets for the SARS-CoV-2 E gene (5'-ACAGGTACGTTAATAGTTAATAGCGT; 5'- ATATTGCAGCAGTACGCACACA) were used. The samples were run in duplicate using the following conditions: 95 °C for 3 min, then 45 cycles of 95 °C for 15 s and 58 °C for 30 s. The plasmid, 2019-nCoV_E Positive Control (IDT, 10006896) was included as a standard to quantify the absolute copies of viral RNA. Statistical analysis of RNA copies was performed in Prism 9 (GraphPad) as an ordinary one-way analysis of variance (ANOVA) with a post-hoc Tukey correction for multiple comparisons between all groups ($n = 5/timepoint$). The adjusted p-values are presented in Fig. 4G together with the relevant data.

For histopathological evaluation, the formalin fixed lung tissues were processed by the Histopathology Core (UTMB) to prepare 5 μm paraffin sections stained with Hematoxylin and Eosin (H&E). The stained lung sections ($n = 5/timepoint$) were evaluated by an experienced pathologist who was blinded to the treatment type. The sections were evaluated for pathologic changes, respiratory epithelial degeneration, and inflammatory infiltrations. Representative images were taken using a Zeiss microscope equipped with an EOS Rebel T3i Canon camera.

Supplementary Material

Refer to Web version on PubMed Central for supplementary material.

Acknowledgements

The authors thank E. A. Pham, J. S. Glenn, M. Smith, P. Humphries, C. Khosla, and N. S. Gray (Stanford University) for helpful discussions. The authors also thank B. Hurst and B. Tarbet, Utah State University, for initial service on antiviral replication assays. MW thanks N. L. Villadsen and F. Ø. Sørensen for helpful discussions. The authors thank Shanghai Chempartner for excellent contract compound synthesis and characterization. A portion of this work was performed at the Sarafan ChEM-H Macromolecular Structure Knowledge Center and the Stanford in vitro Biosafety Level 3 Service Center. The pET His6 TEV LIC cloning vector (2B-T) was a gift from Scott Gradia (Addgene plasmid # 29666 ; http://n2t.net/addgene:29666; RRID:Addgene_29666). Two different SARS-CoV-2-NLuc viruses were used for the project. They were received as gifts from Y. J. Hou and R. Baric (UNC Chapel Hill) or L. Martinez-Sobrido (Texas Biomed), respectively. The A549-ACE2 cells were a gift from R. Bartenschlager (Heidelberg University). The Huh7.5.1-ACE2-TMPRSS2 cells were a gift from A. Puschnik (UCSF).

Funding:

The project is supported by a COVID-19 Response grant from Sarafan ChEM-H and the Innovative Medicines Accelerator (to MZL), a Harrington Scholar-Innovator award (to MZL), Fast Grants 2082 and 2246 for COVID-19 from Emergent Ventures at the Mercatus Center at George Mason University (to MZL and CB), a Stanford-Coulter Translational Research Grant (to MZL and CB), an Antiviral Drug Discovery (AViDD) center funded by NIH/NIAID award U19AI171421 (to MZL, CB, JG, and C-TKT), a grant from the Denver Foundation (to CB), grant NNF18OC0031816 from the Novo Nordisk Foundation and the Stanford Bio-X Program (to MW), a Bio-X Stanford Interdisciplinary Graduate Student Fellowship (to XZ), a E&M Foundation, Houston, postdoctoral fellowship (to PH), a Postdoctoral Fellowship in Translational Medicine by the PhRMA Foundation (to MK), and an anonymous donation to establish the Stanford BSL3 facility. SE and CB are Chan Zuckerberg Biohub investigators. Use of the Stanford Synchrotron Radiation Lightsource, SLAC National Accelerator Laboratory, is supported by the U.S. Department of Energy, Office of Science, Office of Basic Energy Sciences under Contract No. DE-AC02-76SF00515. The SSRL Structural Molecular Biology Program is supported by the DOE Office of Biological and Environmental Research, and by grant P30GM133894 from the National Institute of General Medical Sciences of the National Institutes of Health.

Data and materials availability:

All data associated with this study are in the paper or supplementary materials. Co-crystal structures of SARS-CoV-2 M^{pro} complexed with ML1000, ML1001, ML1006m, ML1006a, ML2006a, ML2006a2, ML,2006a4, ML3006a, or ML4006a have been deposited in the Protein Data Bank with IDs: 7SET, 7SF1, 7SF3, 7U92, 8EZV, 8EZZ, 8F02, 8F2C, and 8F2D. Crystal structures of SARS-CoV-2 M^{pro} S144A complexed with ML1006a or NTV have been deposited in the Protein Data Bank with IDs: 7UUG and 7UUP. DNA plasmids encoding the M^{pro} fusion proteins are available upon request. M^{pro} inhibitors can be ordered from Shanghai Chempartner with reference to the synthesis procedures in data file S2.

References

1. WHO, “COVID-19 Weekly Epidemiological Update - 29 September 2023” (2023).
2. Tenforde MW, Self WH, Gaglani M, Ginde AA, Douin DJ, Talbot HK, Casey JD, Mohr NM, Zepeski A, McNeal T, Ghamande S, Gibbs KW, Files DC, Hager DN, Shehu A, Prekker ME, Frosch AE, Gong MN, Mohamed A, Johnson NJ, Srinivasan V, Steingrub JS, Peltan ID, Brown SM, Martin ET, Monto AS, Khan A, Hough CL, Busse LW, Duggal A, Wilson JG, Qadir N, Chang SY, Mallow C, Rivas C, Babcock HM, Kwon JH, Exline MC, Botros M, Lauring AS, Shapiro NI, Halasa N, Chappell JD, Grijalva CG, Rice TW, Jones ID, Stubblefield WB, Baughman A, Womack KN, Rhoads JP, Lindsell CJ, Hart KW, Zhu Y, Adams K, Surie D, McMorrow ML, Patel MM, Effectiveness of mRNA Vaccination in Preventing COVID-19–Associated Invasive Mechanical

Ventilation and Death — United States, March 2021–January 2022. MMWR Morb. Mortal. Wkly. Rep. 71, 459–465 (2022). [PubMed: 35324878]

3. Nyberg T, Ferguson NM, Nash SG, Webster HH, Flaxman S, Andrews N, Hinsley W, Bernal JL, Kall M, Bhatt S, Blomquist P, Zaidi A, Volz E, Aziz NA, Harman K, Funk S, Abbott S, Lopez Bernal J, Abdul Aziz N, Hope R, Charlett A, Chand M, Ghani AC, Seaman SR, Dabrera G, De Angelis D, Presanis AM, Thelwall S, Comparative analysis of the risks of hospitalisation and death associated with SARS-CoV-2 omicron (B.1.1.529) and delta (B.1.617.2) variants in England: a cohort study. The Lancet 399, 1303–1312 (2022).
4. Deng X, St SE. John HL. Osswald A. O'Brien BS. Banach K Sleeman AK. Ghosh AD. Mesecar SC. Baker, Coronaviruses Resistant to a 3C-Like Protease Inhibitor Are Attenuated for Replication and Pathogenesis, Revealing a Low Genetic Barrier but High Fitness Cost of Resistance. J. Virol 88, 11886–11898 (2014). [PubMed: 25100843]
5. Ullrich S, Nitsche C, The SARS-CoV-2 main protease as drug target. Bioorg. Med. Chem. Lett 30, 127377 (2020). [PubMed: 32738988]
6. Kim Y, Lovell S, Tiew K-C, Mandadapu SR, Alliston KR, Battaile KP, Groutas WC, Chang K-O, Broad-Spectrum Antivirals against 3C or 3C-Like Proteases of Picornaviruses, Noroviruses, and Coronaviruses. J. Virol 86, 11754–11762 (2012). [PubMed: 22915796]
7. Kim Y, Shivanna V, Narayanan S, Prior AM, Weerasekara S, Hua DH, Kankanamalage ACG, Groutas WC, Chang K-O, Broad-Spectrum Inhibitors against 3C-Like Proteases of Feline Coronaviruses and Feline Caliciviruses. J. Virol 89, 4942–4950 (2015). [PubMed: 25694593]
8. Kim Y, Liu H, Galasiti Kankanamalage AC, Weerasekara S, Hua DH, Groutas WC, Chang KO, Pedersen NC, Reversal of the Progression of Fatal Coronavirus Infection in Cats by a Broad-Spectrum Coronavirus Protease Inhibitor. PLoS Pathog. 12, 1–18 (2016).
9. Pedersen NC, Kim Y, Liu H, Galasiti Kankanamalage AC, Eckstrand C, Groutas WC, Bannasch M, Meadows JM, Chang KO, Efficacy of a 3C-like protease inhibitor in treating various forms of acquired feline infectious peritonitis. J. Feline Med. Surg 20, 378–392 (2018). [PubMed: 28901812]
10. Owen DR, Allerton CMN, Anderson AS, Aschenbrenner L, Avery M, Berritt S, Boras B, Cardin RD, Carlo A, Coffman KJ, Dantonio A, Di L, Eng H, Ferre R, Gajiwala KS, Gibson SA, Greasley SE, Hurst BL, Kadar EP, Kalgutkar AS, Lee JC, Lee J, Liu W, Mason SW, Noell S, Novak JJ, Obach RS, Ogilvie K, Patel NC, Pettersson M, Rai DK, Reese MR, Sammons MF, Sathish JG, Singh RSP, Steppan CM, Stewart AE, Tuttle JB, Updyke L, Verhoest PR, Wei L, Yang Q, Zhu Y, An oral SARS-CoV-2 M pro inhibitor clinical candidate for the treatment of COVID-19. Science 374, 1586–1593 (2021). [PubMed: 34726479]
11. Hammond J, Leister-Tebbe H, Gardner A, Abreu P, Bao W, Wisemandle W, Baniecki M, Hendrick VM, Damle B, Simón-Campos A, Pypstra R, Rusnak JM, Oral Nirmatrelvir for High-Risk, Nonhospitalized Adults with Covid-19. N. Engl. J. Med 386, 1397–1408 (2022). [PubMed: 35172054]
12. FDA (US), "Emergency Use Authorization for Paxlovid (nirmatrelvir tablets co-packaged with ritonavir tablets)" (2021).
13. Unoh Y, Uehara S, Nakahara K, Nobori H, Yamatsu Y, Yamamoto S, Maruyama Y, Taoda Y, Kasamatsu K, Suto T, Kouki K, Nakahashi A, Kawashima S, Sanaki T, Toba S, Uemura K, Mizutare T, Ando S, Sasaki M, Orba Y, Sawa H, Sato A, Sato T, Kato T, Tachibana Y, Discovery of S-217622, a Noncovalent Oral SARS-CoV-2 3CL Protease Inhibitor Clinical Candidate for Treating COVID-19. J. Med. Chem 65, 6499–6512 (2022). [PubMed: 35352927]
14. Mukae H, Yotsuyanagi H, Ohmagari N, Doi Y, Sakaguchi H, Sonoyama T, Ichihashi G, Sanaki T, Baba K, Tsuge Y, Uehara T, Efficacy and Safety of Ensitrelvir in Patients With Mild-to-Moderate Coronavirus Disease 2019: The Phase 2b Part of a Randomized, Placebo-Controlled, Phase 2/3 Study. Clin. Infect. Dis 76, 1403–1411 (2022).
15. Yotsuyanagi H, Ohmagari N, Doi Y, Imamura T, Sonoyama T, Ichihashi G, Sanaki T, Tsuge Y, Uehara T, Mukae H, A phase 2/3 study of S-217622 in participants with SARS-CoV-2 infection (Phase 3 part). Medicine (Baltimore) 102, e33024 (2023). [PubMed: 36827007]
16. PDMA (Japan), "Xocova Tablets 125 mg Shionogi & Co., Ltd. review report" (2022).
17. Chen X, Huang X, Ma Q, Kuzmič P, Zhou B, Xu J, Liu B, Jiang H, Zhang W, Yang C, Wu S, Huang J, Li H, Long C, Zhao X, Xu H, Sheng Y, Guo Y, Niu C, Xue L, Xu Y, Liu J, Zhang T, Spencer J, Deng W, Chen S-H, Yang Z, Zhong N, Inhibition mechanism and

antiviral activity of an αketoamide based SARS-CoV-2 main protease inhibitor. bioRxiv, doi: 10.1101/2023.03.09.531862v1 (2023).

18. Wang B, Li H, Cai M, Lin Z, Ou X, Wu S, Cai R, Wei Y, Yang F, Zhu Y, Yang Z, Zhong N, Lin L, Antiviral efficacy of RAY1216 monotherapy and combination therapy with ritonavir in patients with COVID-19: a phase 2, single centre, randomised, double-blind, placebo-controlled trial. eClinicalMedicine 63, 102189 (2023). [PubMed: 37692076]
19. Jiang X, Su H, Shang W, Zhou F, Zhang Y, Zhao W, Zhang Q, Xie H, Jiang L, Nie T, Yang F, Xiong M, Huang X, Li M, Chen P, Peng S, Xiao G, Jiang H, Tang R, Zhang L, Shen J, Xu Y, Structure-based development and preclinical evaluation of the SARS-CoV-2 3C-like protease inhibitor simnotrelvir. Nat. Commun 14, 6463 (2023). [PubMed: 37833261]
20. Cao B, Wang Y, Lu H, Huang C, Yang Y, Shang L, Chen Z, Jiang R, Liu Y, Lin L, Peng P, Wang F, Gong F, Hu H, Cheng C, Yao X, Ye X, Zhou H, Shen Y, Liu C, Wang C, Yi Z, Hu B, Xu J, Gu X, Shen J, Xu Y, Zhang L, Fan J, Tang R, Wang C, Oral Simnotrelvir for Adult Patients with Mild-to-Moderate Covid-19. N. Engl. J. Med 390, 230–241 (2024). [PubMed: 38231624]
21. Janin YL, On the origins of SARS-CoV-2 main protease inhibitors. RSC Med. Chem, 10.1039/D3MD00493G (2023).
22. Tong X, Keung W, Arnold LD, Stevens LJ, Pruijssers AJ, Kook S, Lopatin U, Denison M, Kwong AD, Evaluation of in vitro antiviral activity of SARS-CoV-2 M pro inhibitor pomotrelvir and cross-resistance to nirmatrelvir resistance substitutions. Antimicrob. Agents Chemother, e00840–23 (2023).
23. Mao L, Shaabani N, Zhang X, Jin C, Xu W, Argent C, Kushnareva Y, Powers C, Stegman K, Liu J, Xie H, Xu C, Bao Y, Xu L, Zhang Y, Yang H, Qian S, Hu Y, Shao J, Zhang C, Li T, Li Y, Liu N, Lin Z, Wang S, Wang C, Shen W, Lin Y, Shu D, Zhu Z, Kotoi O, Kerwin L, Han Q, Chumakova L, Teijaro J, Royal M, Brunswick M, Allen R, Ji H, Lu H, Xu X, Olgotrelvir, a dual inhibitor of SARS-CoV-2 Mpro and cathepsin L, as a standalone antiviral oral intervention candidate for COVID-19. Med 5, 42–61.e23 (2024). [PubMed: 38181791]
24. Sedova M, Jaroszewski L, Iyer M, Godzik A, Monitoring for SARS-CoV-2 drug resistance mutations in broad viral populations. bioRxiv, doi: 10.1101/2022.05.27.493798 (2022).
25. Hu Y, Lewandowski EM, Tan H, Zhang X, Morgan RT, Zhang X, Jacobs LMC, Butler SG, Gongora MV, Choy J, Deng X, Chen Y, Wang J, Naturally Occurring Mutations of SARS-CoV-2 Main Protease Confer Drug Resistance to Nirmatrelvir. ACS Cent. Sci, acscentsci.3c00538 (2023).
26. Noske GD, de Souza Silva E, de Godoy MO, Dolci I, Fernandes RS, Guido RVC, Sjö P, Oliva G, Godoy AS, Structural basis of nirmatrelvir and ensitrelvir activity against naturally occurring polymorphisms of the SARS-CoV-2 main protease. J. Biol. Chem 299, 103004 (2023). [PubMed: 36775130]
27. Chen SA, Arutyunova E, Lu J, Khan MB, Rut W, Zmudzinski M, Shahbaz S, Iyyathurai J, Moussa EW, Turner Z, Bai B, Lamer T, Nieman JA, Vederas JC, Julien O, Drag M, Elahi S, Young HS, Lemieux MJ, SARS-CoV-2 M pro Protease Variants of Concern Display Altered Viral Substrate and Cell Host Target Galectin-8 Processing but Retain Sensitivity toward Antivirals. ACS Cent. Sci 9, 696–708 (2023). [PubMed: 37122453]
28. Lee JT, Yang Q, Gribenko A, Perrin BS, Zhu Y, Cardin R, Liberator PA, Anderson AS, Hao L, Genetic Surveillance of SARS-CoV-2 M pro Reveals High Sequence and Structural Conservation Prior to the Introduction of Protease Inhibitor Paxlovid. mBio 13, e00869–22 (2022). [PubMed: 35862764]
29. Ip JD, Wing-Ho Chu A, Chan W-M, Cheuk-Ying Leung R, Umer Abdullah SM, Sun Y, To KK-W, Global prevalence of SARS-CoV-2 3CL protease mutations associated with nirmatrelvir or ensitrelvir resistance. eBioMedicine 91, 104559 (2023). [PubMed: 37060743]
30. Bloom JD, Neher RA, Fitness effects of mutations to SARS-CoV-2 proteins. Virus Evol. 9, vead055 (2023).
31. Flynn JM, Samant N, Schneider-Nachum G, Bakan DT, Yilmaz NK, Schiffer CA, Moquin SA, Dovala D, Bolon DN, Comprehensive fitness landscape of SARS-CoV-2 Mpro reveals insights into viral resistance mechanisms. eLife 11, e77433 (2022). [PubMed: 35723575]
32. FDA (US), Fact Sheet for Healthcare Providers: Emergency Use Authorization for Paxlovid (Revised 02/2023). (2023).

33. Iketani S, Mohri H, Culbertson B, Hong SJ, Duan Y, Luck MI, Annavajhala MK, Guo Y, Sheng Z, Uhlemann A-C, Goff SP, Sabo Y, Yang H, Chavez A, Ho DD, Multiple pathways for SARS-CoV-2 resistance to nirmatrelvir. Nature 613, 558–564 (2023). [PubMed: 36351451]
34. Zhou Y, Gammeltoft KA, Ryberg LA, Pham LV, Tjørnelund HD, Binderup A, Duarte Hernandez CR, Fernandez-Antunez C, Offersgaard A, Fahnøe U, Peters GHJ, Ramirez S, Bukh J, Gottwein JM, Nirmatrelvir-resistant SARS-CoV-2 variants with high fitness in an infectious cell culture system. Sci. Adv 8, eadd7197 (2022).
35. Jochmans D, Liu C, Donckers K, Stoycheva A, Boland S, Stevens SK, De Vita C, Vanmechelen B, Maes P, Trüeb B, Ebert N, Thiel V, De Jonghe S, Vangeel L, Bardiot D, Jekle A, Blatt LM, Beigelman L, Symons JA, Raboisson P, Chaltin P, Marchand A, Neyts J, Deval J, Vandyck K, The Substitutions L50F, E166A, and L167F in SARS-CoV-2 3CLpro Are Selected by a Protease Inhibitor In Vitro and Confer Resistance To Nirmatrelvir. mBio 14, e02815–22 (2023). [PubMed: 36625640]
36. Moghadasi SA, Heilmann E, Khalil AM, Nnabuife C, Kearns FL, Ye C, Moraes SN, Costacurta F, Esler MA, Aihara H, von Laer D, Martinez-Sobrido L, Palzkill T, Amaro RE, Harris RS, Transmissible SARS-CoV-2 variants with resistance to clinical protease inhibitors. Sci. Adv 9, eade8778 (2023).
37. Sasi VM, Ullrich S, Ton J, Fry SE, Johansen-Leete J, Payne RJ, Nitsche C, Jackson CJ, Predicting Antiviral Resistance Mutations in SARS-CoV-2 Main Protease with Computational and Experimental Screening. Biochemistry 61, 2495–2505 (2022). [PubMed: 36326185]
38. Abdelnabi R, Jochmans D, Donckers K, Trüeb B, Ebert N, Weynand B, Thiel V, Neyts J, Nirmatrelvirresistant SARS-CoV-2 is efficiently transmitted in female Syrian hamsters and retains partial susceptibility to treatment. Nat. Commun 14, 2124 (2023). [PubMed: 37059708]
39. Kiso M, Furusawa Y, Uraki R, Imai M, Yamayoshi S, Kawaoka Y, In vitro and in vivo characterization of SARS-CoV-2 strains resistant to nirmatrelvir. Nat. Commun 14, 3952 (2023). [PubMed: 37402789]
40. Kiso M, Yamayoshi S, Iida S, Furusawa Y, Hirata Y, Uraki R, Imai M, Suzuki T, Kawaoka Y, In vitro and in vivo characterization of SARS-CoV-2 resistance to ensitrelvir. Nat. Commun 14, 4231 (2023). [PubMed: 37454219]
41. Heilmann E, Costacurta F, Moghadasi SA, Ye C, Pavan M, Bassani D, Volland A, Ascher C, Weiss AKH, Bante D, Harris RS, Moro S, Rupp B, Martinez-Sobrido L, von Laer D, SARS-CoV-2 3CL pro mutations selected in a VSV-based system confer resistance to nirmatrelvir, ensitrelvir, and GC376. Sci. Transl. Med 15, eabq7360 (2023).
42. Costacurta F, Dodaro A, Bante D, Schöppe H, Sprenger B, Moghadasi SA, Fleischmann J, Pavan M, Bassani D, Menin S, Rauch S, Krismer L, Sauerwein A, Heberle A, Rabensteiner T, Ho J, Harris RS, Stefan E, Schneider R, Kaserer T, Moro S, Von Laer D, Heilmann E, A comprehensive study of SARS-CoV-2 main protease (M pro) inhibitor-resistant mutants selected in a VSV-based system. bioRxiv, doi: 10.1101/2023.09.22.558628 (2023).
43. Lan S, Neilsen G, Slack RL, Cantara WA, Castaner AE, Lorson ZC, Lulkin N, Zhang H, Lee J, Cilento ME, Tedbury PR, Sarafianos SG, Nirmatrelvir Resistance in SARS-CoV-2 Omicron_BA.1 and WA1 Replicons and Escape Strategies. bioRxiv, doi: 10.1101/2022.12.31.522389 (2023).
44. Flynn JM, Huang QYJ, Zvornicanin SN, Schneider-Nachum G, Shaqra AM, Yilmaz NK, Moquin SA, Dovala D, Schiffer CA, Bolon DNA, Systematic Analyses of the Resistance Potential of Drugs Targeting SARS-CoV-2 Main Protease. ACS Infect. Dis 9, 1372–1386 (2023). [PubMed: 37390404]
45. Duan Y, Zhou H, Liu X, Iketani S, Lin M, Zhang X, Bian Q, Wang H, Sun H, Hong SJ, Culbertson B, Mohri H, Luck MI, Zhu Y, Liu X, Lu Y, Yang X, Yang K, Sabo Y, Chavez A, Goff SP, Rao Z, Ho DD, Yang H, Molecular mechanisms of SARS-CoV-2 resistance to nirmatrelvir. Nature 622, 376–382 (2023). [PubMed: 37696289]
46. Moghadasi SA, Biswas RG, Harki DA, Harris RS, Rapid resistance profiling of SARS-CoV-2 protease inhibitors. Npj Antimicrob. Resist 1, 9 (2023).
47. Havranek B, Demissie R, Lee H, Lan S, Zhang H, Sarafianos S, Ayitou AJ-L, Islam SM, Discovery of Nirmatrelvir Resistance Mutations in SARS-CoV-2 3CLpro: A Computational-Experimental Approach. J. Chem. Inf. Model, acs.jcim.3c01269 (2023).

48. Zuckerman NS, Bucris E, Keidar-Friedman D, Amsalem M, Brosh-Nissimov T, Nirmatrelvir Resistance—de Novo E166V/L50V Mutations in an Immunocompromised Patient Treated With Prolonged Nirmatrelvir/Ritonavir Monotherapy Leading to Clinical and Virological Treatment Failure—a Case Report. Clin. Infect. Dis, ciad494 (2023).

49. Hirotsu Y, Kobayashi H, Kakizaki Y, Saito A, Tsutsui T, Kawaguchi M, Shimamura S, Hata K, Hanawa S, Toyama J, Miyashita Y, Omata M, Multidrug-resistant mutations to antiviral and antibody therapy in an immunocompromised patient infected with SARS-CoV-2. Med 4, 813–824.e4 (2023). [PubMed: 37683636]

50. Kurt Yilmaz N, Swanstrom R, Schiffer CA, Improving Viral Protease Inhibitors to Counter Drug Resistance. Trends Microbiol. 24, 547–557 (2016). [PubMed: 27090931]

51. Bacon BR, Gordon SC, Lawitz E, Marcellin P, Vierling JM, Zeuzem S, Poordad F, Goodman ZD, Sings HL, Boparai N, Burroughs M, Brass CA, Albrecht JK, Esteban R, Boceprevir for previously treated chronic HCV genotype 1 infection. N. Engl. J. Med 364, 1207–1217 (2011). [PubMed: 21449784]

52. Poordad F, McCone J, Bacon BR, Bruno S, Manns MP, Sulkowski MS, Jacobson IM, Reddy KR, Goodman ZD, Boparai N, DiNubile MJ, Sniukiene V, Brass CA, Albrecht JK, Bronowicki J-P, Boceprevir for Untreated Chronic HCV Genotype 1 Infection. N. Engl. J. Med 364, 1195–1206 (2011). [PubMed: 21449783]

53. Lewis SD, Ng AS, Lyle EA, Mellott MJ, Appleby SD, Brady SF, Stauffer KJ, Sisko JT, Mao S-S, Veber DF, Nutt RF, Lynch JJ, Cook JJ, Gardll SJ, Shafer JA, Inhibition of Thrombin by Peptides Containing Lysyl-α-Keto Carbonyl Derivatives. Thromb. Haemost 74, 1107–1112 (1995). [PubMed: 8560421]

54. Perni RB, Pitlik J, Britt SD, Court JJ, Courtney LF, Deininger DD, Farmer LJ, Gates CA, Harbeson SL, Levin RB, Lin C, Lin K, Moon Y-C, Luong Y-P, O'Malley ET, Rao BG, Thomson JA, Tung RD, Van Drie JH, Wei Y, Inhibitors of hepatitis C virus NS3·4A protease 2. Warhead SAR and optimization. Bioorg. Med. Chem. Lett 14, 1441–1446 (2004). [PubMed: 15006379]

55. Brady SF, Sisko JT, Stauffer KJ, Colton CD, Qiu H, Lewis SD, Ng AS, Shafer JA, Bogusky MJ, Veber DF, Nutt RF, Amide and α-keto carbonyl inhibitors of thrombin based on arginine and lysine: Synthesis, stability and biological characterization. Bioorg. Med. Chem 3, 1063–1078 (1995). [PubMed: 7582980]

56. Zhang L, Lin D, Kusov Y, Nian Y, Ma Q, Wang J, von Brunn A, Leyssen P, Lanko K, Neyts J, de Wilde A, Snijder EJ, Liu H, Hilgenfeld R, α-Ketoamides as Broad-Spectrum Inhibitors of Coronavirus and Enterovirus Replication: Structure-Based Design, Synthesis, and Activity Assessment. J. Med. Chem 63, 4562–4578 (2020). [PubMed: 32045235]

57. Zhang L, Lin D, Sun X, Curth U, Drosten C, Sauerhering L, Becker S, Rox K, Hilgenfeld R, Crystal structure of SARS-CoV-2 main protease provides a basis for design of improved α-ketoamide inhibitors. Science 368, 409–412 (2020). [PubMed: 32198291]

58. Yang S, Chen SJ, Hsu MF, Wu JD, Tseng CTK, Liu YF, Chen HC, Kuo CW, Wu CS, Chang LW, Chen WC, Liao SY, Chang TY, Hung HH, Shr HL, Liu CY, Huang YA, Chang LY, Hsu JC, Peters CJ, Wang AHJ, Hsu MC, Synthesis, crystal structure, structure-activity relationships, and antiviral activity of a potent SARS coronavirus 3CL protease inhibitor. J. Med. Chem 49, 4971–4980 (2006). [PubMed: 16884309]

59. Qiao J, Li Y-S, Zeng R, Liu F-L, Luo R-H, Huang C, Wang Y-F, Zhang J, Quan B, Shen C, Mao X, Liu X, Sun W, Yang W, Ni X, Wang K, Xu L, Duan Z-L, Zou Q-C, Zhang H-L, Qu W, Long Y-H-P, Li M-H, Yang R-C, Liu X, You J, Zhou Y, Yao R, Li W-P, Liu J-M, Chen P, Liu Y, Lin G-F, Yang X, Zou J, Li L, Hu Y, Lu G-W, Li W-M, Wei Y-Q, Zheng Y-T, Lei J, Yang S, SARS-CoV-2 M pro inhibitors with antiviral activity in a transgenic mouse model. Science 371, 1374–1378 (2021). [PubMed: 33602867]

60. Dai W, Zhang B, Jiang X-M, Su H, Li J, Zhao Y, Xie X, Jin Z, Peng J, Liu F, Li C, Li Y, Bai F, Wang H, Cheng X, Cen X, Hu S, Yang X, Wang J, Liu X, Xiao G, Jiang H, Rao Z, Zhang L-K, Xu Y, Yang H, Liu H, Structure-based design of antiviral drug candidates targeting the SARS-CoV-2 main protease. Science 368, 1331–1335 (2020). [PubMed: 32321856]

61. Gampe C, Verma VA, Curse or Cure? A Perspective on the Developability of Aldehydes as Active Pharmaceutical Ingredients. J. Med. Chem 63, 14357–14381 (2020). [PubMed: 32916044]

62. Vasudevan A, Argiriadi MA, Baranczak A, Friedman MM, Gavrilyuk J, Hobson AD, Hulce JJ, Osman S, Wilson NS, Covalent Binders in Drug Discovery (Elsevier B.V., 2019; 10.1016/bs.pmch.2018.12.002)vol. 58 of Progress in Medicinal Chemistry.

63. Jin Z, Du X, Xu Y, Deng Y, Liu M, Zhao Y, Zhang B, Li X, Zhang L, Peng C, Duan Y, Yu J, Wang L, Yang K, Liu F, Jiang R, Yang X, You T, Liu X, Yang X, Bai F, Liu H, Liu X, Guddat LW, Xu W, Xiao G, Qin C, Shi Z, Jiang H, Rao Z, Yang H, Structure of Mpro from SARS-CoV-2 and discovery of its inhibitors. Nature 582, 289–293 (2020). [PubMed: 32272481]

64. Hsu M, Kuo C, Chang K-T, Chang H-C, Chou C, Ko T, Shr H, Chang G, Wang AH-J, Liang P, Mechanism of the Maturation Process of SARS-CoV 3CL Protease. J. Biol. Chem 280, 31257–31266 (2005). [PubMed: 15788388]

65. Fu L, Ye F, Feng Y, Yu F, Wang Q, Wu Y, Zhao C, Sun H, Huang B, Niu P, Song H, Shi Y, Li X, Tan W, Qi J, Gao GF, Both Boceprevir and GC376 efficaciously inhibit SARS-CoV-2 by targeting its main protease. Nat. Commun 11, 4417 (2020). [PubMed: 32887884]

66. Ma C, Sacco MD, Hurst B, Townsend JA, Hu Y, Szeto T, Zhang X, Tarbet B, Marty MT, Chen Y, Wang J, Boceprevir GC-376, and calpain inhibitors II, XII inhibit SARS-CoV-2 viral replication by targeting the viral main protease. Cell Res. 30, 678–692 (2020). [PubMed: 32541865]

67. Anson B, Chapman M, Lendy E, Pshenychnyi S, D'Aquila R, Satchell K, Mesecar A, Broad-spectrum inhibition of coronavirus main and papain-like proteases by HCV drugs. Res. Sq, doi: 10.21203/rs.3.rs26344/v1 (2020).

68. Chuck C-P, Chow H-F, Wan DC-C, Wong K-B, Profiling of Substrate Specificities of 3C-Like Proteases from Group 1, 2a, 2b, and 3 Coronaviruses. PLoS ONE 6, e27228 (2011).

69. Tan J, George S, Kusov Y, Perbandt M, Anemuller S, Mesters JR, Norder H, Coutard B, Lacroix C, Leyssen P, Neyts J, Hilgenfeld R, 3C Protease of Enterovirus 68: Structure-Based Design of Michael Acceptor Inhibitors and Their Broad-Spectrum Antiviral Effects against Picornaviruses. J. Virol 87, 4339–4351 (2013). [PubMed: 23388726]

70. Matthews DA, Dragovich PS, Webber SE, Fuhrman SA, Patick AK, Zalman LS, Hendrickson TF, Love RA, Prins TJ, Marakovits JT, Zhou R, Tikhe J, Ford CE, Meador JW, Ferre RA, Brown EL, Binford SL, Brothers MA, DeLisle DM, Worland ST, Structure-assisted design of mechanism-based irreversible inhibitors of human rhinovirus 3C protease with potent antiviral activity against multiple rhinovirus serotypes. Proc. Natl. Acad. Sci 96, 11000–11007 (1999). [PubMed: 10500114]

71. Dragovich PS, Prins TJ, Zhou R, Webber SE, Marakovits JT, Fuhrman SA, Patick AK, Matthews DA, Lee CA, Ford CE, Burke BJ, Rejto PA, Hendrickson TF, Tuntland T, Brown EL, Meador JW, Ferre RA, Harr JEV, Kosa MB, Worland ST, Structure-based design, synthesis, and biological evaluation of irreversible human rhinovirus 3C protease inhibitors. 4. Incorporation of P1 lactam moieties as L-glutamine replacements. J. Med. Chem 42, 1213–1224 (1999). [PubMed: 10197965]

72. Patick AK, Brothers MA, Maldonado F, Binford S, Maldonado O, Fuhrman S, Petersen A, Smith GJ, Zalman LS, Burns-Naas LA, Tran JQ, In vitro antiviral activity and single-dose pharmacokinetics in humans of a novel, orally bioavailable inhibitor of human rhinovirus 3C protease. Antimicrob. Agents Chemother. 49, 2267–2275 (2005). [PubMed: 15917520]

73. Rut W, Groborz K, Zhang L, Sun X, Zmudzinski M, Pawlik B, Wang X, Jochmans D, Neyts J, Młynarski W, Hilgenfeld R, Drag M, SARS-CoV-2 Mpro inhibitors and activity-based probes for patient-sample imaging. Nat. Chem. Biol 17, 222–228 (2021). [PubMed: 33093684]

74. Shultz MD, Two Decades under the Influence of the Rule of Five and the Changing Properties of Approved Oral Drugs. J. Med. Chem 62, 1701–1714 (2019). [PubMed: 30212196]

75. Robello M, Barresi E, Baglini E, Salerno S, Taliani S, Settimo FD, The Alpha Keto Amide Moiety as a Privileged Motif in Medicinal Chemistry: Current Insights and Emerging Opportunities. J. Med. Chem 64, 3508–3545 (2021). [PubMed: 33764065]

76. Kahn K, Bruice TC, α-Ketoamides and α-ketocarbonyls: Conformational analysis and development of allatom OPLS force field. Bioorg. Med. Chem 8, 1881–1891 (2000). [PubMed: 11003132]

77. Wang Y, Yang B, Zhai Y, Yin Z, Sun Y, Rao Z, Peptidyl Aldehyde NK-1.8k Suppresses Enterovirus 71 and Enterovirus 68 Infection by Targeting Protease 3C. Antimicrob. Agents Chemother. 59, 2636–2646 (2015). [PubMed: 25691647]

78. Wang H, He S, Deng W, Zhang Y, Li G, Sun J, Zhao W, Guo Y, Yin Z, Li D, Shang L, Comprehensive Insights into the Catalytic Mechanism of Middle East Respiratory Syndrome 3C-Like Protease and Severe Acute Respiratory Syndrome 3C-Like Protease. ACS Catal. 10, 5871–5890 (2020). [PubMed: 32391184]

79. Bai B, Arutyunova E, Khan MB, Lu J, Joyce MA, Saffran HA, Shields JA, Kandadai AS, Belovodskiy A, Hena M, Vuong W, Lamer T, Young HS, Vederas JC, Tyrrell DL, Lemieux MJ, Nieman JA, Peptidomimetic nitrile warheads as SARS-CoV-2 3CL protease inhibitors. RSC Med. Chem 12, 1722–1730 (2021). [PubMed: 34778773]

80. Sathish JG, Bhatt S, DaSilva JK, Flynn D, Jenkinson S, Kalgutkar AS, Liu M, Manickam B, Pinkstaff J, Reagan WJ, Shirai N, Shoieb AM, Sirivelu M, Vispute S, Vitsky A, Walters K, Wisialowski TA, Updyke LW, Comprehensive Nonclinical Safety Assessment of Nirmatrelvir Supporting Timely Development of the SARS-COV-2 Antiviral Therapeutic, PaxlovidTM. Int. J. Toxicol 41, 276–290 (2022). [PubMed: 35603517]

81. Dahl G, Akerud T, Pharmacokinetics and the drug-target residence time concept. Drug Discov. Today 18, 697–707 (2013). [PubMed: 23500610]

82. Steuten K, Kim H, Widen JC, Babin BM, Onguka O, Lovell S, Bolgi O, Cerikan B, Neufeldt CJ, Cortese M, Muir RK, Bennett JM, Geiss-Friedlander R, Peters C, Bartenschlager R, Bogyo M, Challenges for Targeting SARS-CoV-2 Proteases as a Therapeutic Strategy for COVID-19. ACS Infect. Dis 7, 1457–1468 (2021). [PubMed: 33570381]

83. Liverton NJ, Carroll SS, DiMuzio J, Fandozzi C, Graham DJ, Hazuda D, Holloway MK, Ludmerer SW, McCauley JA, McIntyre CJ, Olsen DB, Rudd MT, Stahlhut M, Vacca JP, MK-7009, a Potent and Selective Inhibitor of Hepatitis C Virus NS3/4A Protease. Antimicrob. Agents Chemother. 54, 305–311 (2010). [PubMed: 19841155]

84. Mason S, Devincenzo JP, Toovey S, Wu JZ, Whitley RJ, Comparison of antiviral resistance across acute and chronic viral infections. Antiviral Res. 158, 103–112 (2018). [PubMed: 30086337]

85. Shaqra AM, Zvornicanin SN, Huang QYJ, Lockbaum GJ, Knapp M, Tandeske L, Bakan DT, Flynn J, Bolon DNA, Moquin S, Dovala D, Kurt Yilmaz N, Schiffer CA, Defining the substrate envelope of SARS-CoV-2 main protease to predict and avoid drug resistance. Nat. Commun 13, 3556 (2022). [PubMed: 35729165]

86. Barrila J, Bacha U, Freire E, Long-Range Cooperative Interactions Modulate Dimerization in SARS 3CLpro. Biochemistry 45, 14908–14916 (2006). [PubMed: 17154528]

87. Boras B, Jones RM, Anson BJ, Arenson D, Aschenbrenner L, Bakowski MA, Beutler N, Binder J, Chen E, Eng H, Hammond H, Hammond J, Haupt RE, Hoffman R, Kadar EP, Kania R, Kimoto E, Kirkpatrick MG, Lanyon L, Lendy EK, Lillis JR, Logue J, Luthra SA, Ma C, Mason SW, McGrath ME, Noell S, Obach RS, O' Brien MN, O'Connor R, Ogilvie K, Owen D, Pettersson M, Reese MR, Rogers TF, Rosales R, Rossulek MI, Sathish JG, Shirai N, Steppan C, Ticehurst M, Updyke LW, Weston S, Zhu Y, White KM, García-Sastre A, Wang J, Chatterjee AK, Mesecar AD, Frieman MB, Anderson AS, Allerton C, Preclinical characterization of an intravenous coronavirus 3CL protease inhibitor for the potential treatment of COVID19. Nat. Commun 12, 6055 (2021). [PubMed: 34663813]

88. Yang KS, Leeuwon SZ, Xu S, Liu WR, Evolutionary and Structural Insights about Potential SARSCoV-2 Evasion of Nirmatrelvir. J. Med. Chem 65, 8686–8698 (2022). [PubMed: 35731933]

89. Cheng SC, Chang GG, Chou CY, Mutation of glu-166 blocks the substrate-induced dimerization of SARS coronavirus main protease. Biophys. J 98, 1327–1336 (2010). [PubMed: 20371333]

90. Ferreira JC, Fadl S, Rabeh WM, Key dimer interface residues impact the catalytic activity of 3CLpro, the main protease of SARS-CoV-2. J. Biol. Chem 298, 102023 (2022). [PubMed: 35568197]

91. Boby ML, Fearon D, Ferla M, Filep M, Koekemoer L, Robinson MC, The COVID Moonshot Consortium, J. D. Chodera, A. A. Lee, N. London, A. Von Delft, F. Von Delft, Open science discovery of potent noncovalent SARS-CoV-2 main protease inhibitors. Science 382, eabo7201 (2023).

92. Abdelnabi R, Foo CS, Kaptein SJF, Boudewijns R, Vangeel L, De Jonghe S, Jochmans D, Weynand B, Neyts J, A SCID Mouse Model To Evaluate the Efficacy of Antivirals against SARS-CoV-2 Infection. J. Virol 96, e00758–22 (2022). [PubMed: 35924921]

93. Abdelnabi R, Foo CS, Jochmans D, Vangeel L, De Jonghe S, Augustijns P, Mols R, Weynand B, Wattanakul T, Hoglund RM, Tarning J, Mowbray CE, Sjö P, Escudié F, Scandale I, Chatelain E, Neyts J, The oral protease inhibitor (PF-07321332) protects Syrian hamsters against infection with SARS-CoV2 variants of concern. Nat. Commun 13, 719 (2022). [PubMed: 35169114]

94. Quan BX, Shuai H, Xia AJ, Hou Y, Zeng R, Liu XL, Lin GF, Qiao JX, Li WP, Wang FL, Wang K, Zhou RJ, Yuen TTT, Chen MX, Yoon C, Wu M, Zhang SY, Huang C, Wang YF, Yang W, Tian C, Li WM, Wei YQ, Yuen KY, Chan JFW, Lei J, Chu H, Yang S, An orally available Mpro inhibitor is effective against wild-type SARS-CoV-2 and variants including Omicron. Nat. Microbiol 7, 716–725 (2022). [PubMed: 35477751]

95. Huang C, Shuai H, Qiao J, Hou Y, Zeng R, Xia A, Xie L, Fang Z, Li Y, Yoon C, Huang Q, Hu B, You J, Quan B, Zhao X, Guo N, Zhang S, Ma R, Zhang J, Wang Y, Yang R, Zhang S, Nan J, Xu H, Wang F, Lei J, Chu H, Yang S, A new generation Mpro inhibitor with potent activity against SARS-CoV-2 Omicron variants. Signal Transduct. Target. Ther 8, 128 (2023). [PubMed: 36928316]

96. Cox RM, Lieber CM, Wolf JD, Karimi A, Lieberman NAP, Sticher ZM, Roychoudhury P, Andrews MK, Krueger RE, Natchus MG, Painter GR, Kolykhalov AA, Greninger AL, Plemper RK, Comparing molnupiravir and nirmatrelvir/ritonavir efficacy and the effects on SARS-CoV-2 transmission in animal models. Nat. Commun 14, 4731 (2023). [PubMed: 37550333]

97. Soumana DI, Kurt Yilmaz N, Prachanronarong KL, Aydin C, Ali A, Schiffer CA, Structural and Thermodynamic Effects of Macrocyclization in HCV NS3/4A Inhibitor MK-5172. ACS Chem. Biol 11, 900–909 (2016).

98. Chang KO, Kim Y, Lovell S, Rathnayake AD, Groutas WC, Antiviral drug discovery: Norovirus proteases and development of inhibitors. Viruses 11, 1–14 (2019).

99. Fang Z, Song Y, Zhan P, Zhang Q, Liu X, Conformational restriction: an effective tactic in 'follow-on'based drug discovery. Future Med. Chem 6, 885–901 (2014). [PubMed: 24962281]

100. Cowell SM, Lee YS, Cain JP, Hruby VJ, Exploring Ramachandran and Chi Space: Conformationally Constrained Amino Acids and Peptides in the Design of Bioactive Polypeptide Ligands. Curr. Med. Chem 11, 2785–2798 (2012).

101. Weerawarna P, Main Proteases of Key RNA Viruses, Including Coronavirus, Recognize P2 Residues in the Polyproline Type II Conformation: Harnessing Proline's Unique Conformation for Protease Inhibitors. ChemRxiv, doi: 10.26434/chemrxiv-2023-lfxqv-v2 (2023).

102. Bauer MR, Di Fruscia P, Lucas SCC, Michaelides IN, Nelson JE, Storer RI, Whitehurst BC, Put a ring on it: application of small aliphatic rings in medicinal chemistry. RSC Med. Chem 12, 448–471 (2021). [PubMed: 33937776]

103. Copeland RA, The drug–target residence time model: a 10-year retrospective. Nat. Rev. Drug Discov. 15, 87–95 (2016). [PubMed: 26678621]

104. Pandit JA, Radin JM, Chiang DC, Spencer EG, Pawelek JB, Diwan M, Roumani L, Mina MJ, The Coronavirus Disease 2019 Rebound Study: A Prospective Cohort Study to Evaluate Viral and Symptom Rebound Differences in Participants Treated With Nirmatrelvir Plus Ritonavir Versus Untreated Controls. Clin. Infect. Dis 77, 25–31 (2023). [PubMed: 36810665]

105. Edelstein GE, Boucau J, Uddin R, Marino C, Liew MY, Barry M, Choudhary MC, Gilbert RF, Reynolds Z, Li Y, Tien D, Sagar S, Vyas TD, Kawano Y, Sparks JA, Hammond SP, Wallace Z, Vyas JM, Barczak AK, Lemieux JE, Li JZ, Siedner MJ, SARS-CoV-2 Virologic Rebound With Nirmatrelvir–Ritonavir Therapy: An Observational Study. Ann. Intern. Med 176, 1577–1585 (2023). [PubMed: 37956428]

106. Zuo X, Mattern MR, Tan R, Li S, Hall J, Sterner DE, Shoo J, Tran H, Lim P, Sarafianos SG, Kazi L, Navas-Martin S, Weiss SR, Butt TR, Expression and purification of SARS coronavirus proteins using SUMO-fusions. Protein Expr. Purif 42, 100–110 (2005). [PubMed: 15939295]

107. Goličnik M, Exact and approximate solutions for the decades-old Michaelis-Menten equation: Progress-curve analysis through integrated rate equations. Biochem. Mol. Biol. Educ 39, 117–125 (2011). [PubMed: 21445903]

108. Copeland RA, Evaluation of Enzyme Inhibitors in Drug Discovery: A Guide for Medicinal Chemists and Pharmacologists (Wiley, ed. 2, 2013; https://onlinelibrary.wiley.com/doi/book/10.1002/9781118540398).

109. Cheng Y-C, Prusoff WH, Relationship between the inhibition constant (KI) and the concentration of inhibitor which causes 50 per cent inhibition (I50) of an enzymatic reaction. Biochem. Pharmacol 22, 3099–3108 (1973). [PubMed: 4202581]

110. Johnson KA, Simpson ZB, Blom T, Global Kinetic Explorer: A new computer program for dynamic simulation and fitting of kinetic data. Anal. Biochem 387, 20–29 (2009). [PubMed: 19154726]

111. Russi S, Song J, Mcphillips SE, Cohen AE, The Stanford Automated Mounter: Pushing the limits of sample exchange at the SSRL macromolecular crystallography beamlines. J. Appl. Crystallogr 49, 622–626 (2016). [PubMed: 27047309]

112. Kabsch W, XDS. Acta Crystallogr. D Biol. Crystallogr 66, 125–132 (2010).

113. Winter G, Waterman DG, Parkhurst JM, Brewster AS, Gildea RJ, Gerstel M, Fuentes-Montero L, Vollmar M, Michels-Clark T, Young ID, Sauter NK, Evans G, DIALS: Implementation and evaluation of a new integration package. Acta Crystallogr. Sect. Struct. Biol 74, 85–97 (2018).

114. Evans P, Scaling and assessment of data quality. Acta Crystallogr. D Biol. Crystallogr 62, 72–82 (2006). [PubMed: 16369096]

115. Evans PR, Murshudov GN, How good are my data and what is the resolution? Acta Crystallogr. D Biol. Crystallogr. 69, 1204–1214 (2013).

116. Collaborative Computational Project, The CCP4 suite: Programs for protein crystallography. Acta Crystallogr. D Biol. Crystallogr 50, 760–763 (1994). [PubMed: 15299374]

117. Potterton L, Agirre J, Ballard C, Cowtan K, Dodson E, Evans PR, Jenkins HT, Keegan R, Krissinel E, Stevenson K, Lebedev A, McNicholas SJ, Nicholls RA, Noble M, Pannu NS, Roth C, Sheldrick G, Skubak P, Turkenburg J, Uski V, von Delft F, Waterman D, Wilson K, Winn M, Wojdyr M, CCP4i2: the new graphical user interface to the CCP4 program suite. Acta Crystallogr. Sect. Struct. Biol 74, 68–84 (2018).

118. McCoy AJ, Grosse-Kunstleve RW, Adams PD, Winn MD, Storoni LC, Read RJ, Phaser crystallographic software. J. Appl. Crystallogr 40, 658–674 (2007). [PubMed: 19461840]

119. Murshudov GN, Vagin AA, Dodson EJ, Refinement of macromolecular structures by the maximumlikelihood method. Acta Crystallogr. D Biol. Crystallogr 53, 240–255 (1997). [PubMed: 15299926]

120. Emsley P, Cowtan K, Coot: Model-building tools for molecular graphics. Acta Crystallogr. D Biol. Crystallogr. 60, 2126–2132 (2004).

121. Klein S, Cortese M, Winter SL, Wachsmuth-Melm M, Neufeldt CJ, Cerikan B, Stanifer ML, Boulant S, Bartenschlager R, Chlanda P, SARS-CoV-2 structure and replication characterized by in situ cryoelectron tomography. Nat. Commun 11, 1–10 (2020). [PubMed: 31911652]

122. Wang R, Simoneau CR, Kulsuptrakul J, Bouhaddou M, Travisano KA, Hayashi JM, CarlsonStevermer J, Zengel JR, Richards CM, Fozouni P, Oki J, Rodriguez L, Joehnk B, Walcott K, Holden K, Sil A, Carette JE, Krogan NJ, Ott M, Puschnik AS, Genetic Screens Identify Host Factors for SARSCoV-2 and Common Cold Coronaviruses. Cell 184, 106–119.e14 (2021). [PubMed: 33333024]

123. Dinnon KH, Leist SR, Schäfer A, Edwards CE, Martinez DR, Montgomery SA, West A, Yount BL, Hou YJ, Adams LE, Gully KL, Brown AJ, Huang E, Bryant MD, Choong IC, Glenn JS, Gralinski LE, Sheahan TP, Baric RS, A mouse-adapted model of SARS-CoV-2 to test COVID-19 countermeasures. Nature 586, 560–566 (2020). [PubMed: 32854108]

124. Ye C, Chiem K, Park J-G, Silvas JA, Morales Vasquez D, Sourimant J, Lin MJ, Greninger AL, Plemper RK, Torrelles JB, Kobie JJ, Walter MR, De La Torre JC, Martinez-Sobrido L, Analysis of SARS-CoV-2 infection dynamic in vivo using reporter-expressing viruses. Proc. Natl. Acad. Sci 118, e2111593118 (2021). [PubMed: 34561300]

125. Case JB, Bailey AL, Kim AS, Chen RE, Diamond MS, Growth, detection, quantification, and inactivation of SARS-CoV-2. Virology 548, 39–48 (2020). [PubMed: 32838945]

126. Di L, Umland JP, Trapa PE, Maurer TS, Impact of Recovery on Fraction Unbound Using Equilibrium Dialysis. J. Pharm. Sci 101, 1327–1335 (2012). [PubMed: 22161810]

127. Di L, Breen C, Chambers R, Eckley ST, Fricke R, Ghosh A, Harradine P, Kalvass JC, Ho S, Lee CA, Marathe P, Perkins EJ, Qian M, Tse S, Yan Z, Zamek-Gliszczynski MJ, Industry Perspective on Contemporary Protein-Binding Methodologies: Considerations for Regulatory

Drug-Drug Interaction and Related Guidelines on Highly Bound Drugs. J. Pharm. Sci 106, 3442–3452 (2017). [PubMed: 28927987]

128. Hossain MA, Tran T, Chen T, Mikus G, Greenblatt DJ, Inhibition of human cytochromes P450 in vitro by ritonavir and cobicistat. J. Pharm. Pharmacol 69, 1786–1793 (2017). [PubMed: 28960344]
129. Zhang Y, Huo M, Zhou J, Xie S, PKSolver: An add-in program for pharmacokinetic and pharmacodynamic data analysis in Microsoft Excel. Comput. Methods Programs Biomed. 99, 306–314 (2010). [PubMed: 20176408]
130. Hill A, Van Der Lugt J, Sawyer W, Boffito M, How much ritonavir is needed to boost protease inhibitors? Systematic review of 17 dose-ranging pharmacokinetic trials. Aids 23, 2237–2245 (2009). [PubMed: 19809270]
131. Nair A, Jacob S, A simple practice guide for dose conversion between animals and human. J. Basic Clin. Pharm 7, 27 (2016). [PubMed: 27057123]
132. Leist SR, Dinnon KH, Schäfer A, Tse LV, Okuda K, Hou YJ, West A, Edwards CE, Sanders W, Fritch EJ, Gully KL, Scobey T, Brown AJ, Sheahan TP, Moorman NJ, Boucher RC, Gralinski LE, Montgomery SA, Baric RS, A Mouse-Adapted SARS-CoV-2 Induces Acute Lung Injury and Mortality in Standard Laboratory Mice. Cell 183, 1070–1085 (2020). [PubMed: 33031744]
133. Tseng C-TK, Huang C, Newman P, Wang N, Narayanan K, Watts DM, Makino S, Packard MM, Zaki SR, Chan T, Peters CJ, Severe Acute Respiratory Syndrome Coronavirus Infection of Mice Transgenic for the Human Angiotensin-Converting Enzyme 2 Virus Receptor. J. Virol 81, 1162–1173 (2007). [PubMed: 17108019]
134. Tseng C-T, Sbrana E, Iwata-Yoshikawa N, Newman PC, Garron T, Atmar RL, Peters CJ, Couch RB, Immunization with SARS Coronavirus Vaccines Leads to Pulmonary Immunopathology on Challenge with the SARS Virus. PLoS ONE 7, e35421 (2012). [PubMed: 22536382]
135. Kneller DW, Galanie S, Phillips G, O'Neill HM, Coates L, Kovalevsky A, Malleability of the SARSCoV-2 3CL Mpro Active-Site Cavity Facilitates Binding of Clinical Antivirals. Structure 28, 1313–1320.e3 (2020). [PubMed: 33152262]
136. Bai Y, Ye F, Feng Y, Liao H, Song H, Qi J, Gao GF, Tan W, Fu L, Shi Y, Structural basis for the inhibition of the SARS-CoV-2 main protease by the anti-HCV drug narlaprevir. Signal Transduct. Target. Ther 6, 2020–2022 (2021).
137. Andi B, Kumaran D, Kreitler DF, Soares AS, Keereetaweep J, Jakoncic J, Lazo EO, Shi W, Fuchs MR, Sweet RM, Shanklin J, Adams PD, Schmidt JG, Head MS, Mcsweeney S, Hepatitis C virus NS3/4A inhibitors and other drug-like compounds as covalent binders of SARS-CoV-2 main protease. Sci. Rep 12, 1–12 (2022). [PubMed: 34992227]
138. Jaskolski M, Dauter Z, Shabalin IG, Gilski M, Brzezinski D, Kowiel M, Rupp B, Wlodawer A, Crystallographic models of SARS-CoV-2 3CLpro: in-depth assessment of structure quality and validation. IUCrJ 8, 238–256 (2021).
139. Zimmerman MI, Porter JR, Ward MD, Singh S, Vithani N, Meller A, Mallimadugula UL, Kuhn CE, Borowsky JH, Wiewiora RP, Hurley MFD, Harbison AM, Fogarty CA, Coffland JE, Fadda E, Voelz VA, Chodera JD, Bowman GR, SARS-CoV-2 simulations go exascale to predict dramatic spike opening and cryptic pockets across the proteome. Nat. Chem 13, 651–659 (2021). [PubMed: 34031561]
140. Singh RSP, Toussi SS, Hackman F, Chan PL, Rao R, Allen R, Van Eyck L, Pawlak S, Kadar EP, Clark F, Shi H, Anderson AS, Binks M, Menon S, Nucci G, Bergman A, Innovative Randomized Phase I Study and Dosing Regimen Selection to Accelerate and Inform Pivotal COVID-19 Trial of Nirmatrelvir. Clin. Pharmacol. Ther 112, 101–111 (2022). [PubMed: 35388471]
141. Grebennikov D, Kholodareva E, Sazonov I, Karsonova A, Meyerhans A, Bocharov G, Intracellular Life Cycle Kinetics of SARS-CoV-2 Predicted Using Mathematical Modelling. Viruses 13, 1735 (2021). [PubMed: 34578317]
142. Zhao Y, Fang C, Zhang Q, Zhang R, Zhao X, Duan Y, Wang H, Zhu Y, Feng L, Zhao J, Shao M, Yang X, Zhang L, Peng C, Yang K, Ma D, Rao Z, Yang H, Crystal structure of SARS-CoV-2 main protease in complex with protease inhibitor PF-07321332. Protein Cell 13, 689–693 (2022). [PubMed: 34687004]

143. Wasserman HH, Ho W-B, (Cyanomethylene)phosphoranes as Novel Carbonyl 1,1-Dipole Synthons: An Efficient Synthesis of .alpha.-Keto Acids, Esters, and Amides. J. Org. Chem 59, 4364–4366 (1994).

144. Dafydd Rhys O, Pettersson MY, Reese MR, Sammons MF, Tuttle JB, Verhoes PR, Wei L, Yang Q, Yang X, WO 2021/250648 A1 (2021).

145. Wedler HB, Palazzo TA, Pemberton RP, Hamann CS, Kurth MJ, Tantillo DJ, Predicting hydration propensities of biologically relevant α-ketoamides. Bioorg. Med. Chem. Lett 25, 4153–4157 (2015). [PubMed: 26306983]

146. Howe AYM, Venkatraman S, The Discovery and Development of Boceprevir: A Novel, First-generation Inhibitor of the Hepatitis C Virus NS3/4A Serine Protease. J. Clin. Transl. Hepatol 1, 22–32 (2013).

147. FDA (US), “Application 202258Orig1s000” (2009).

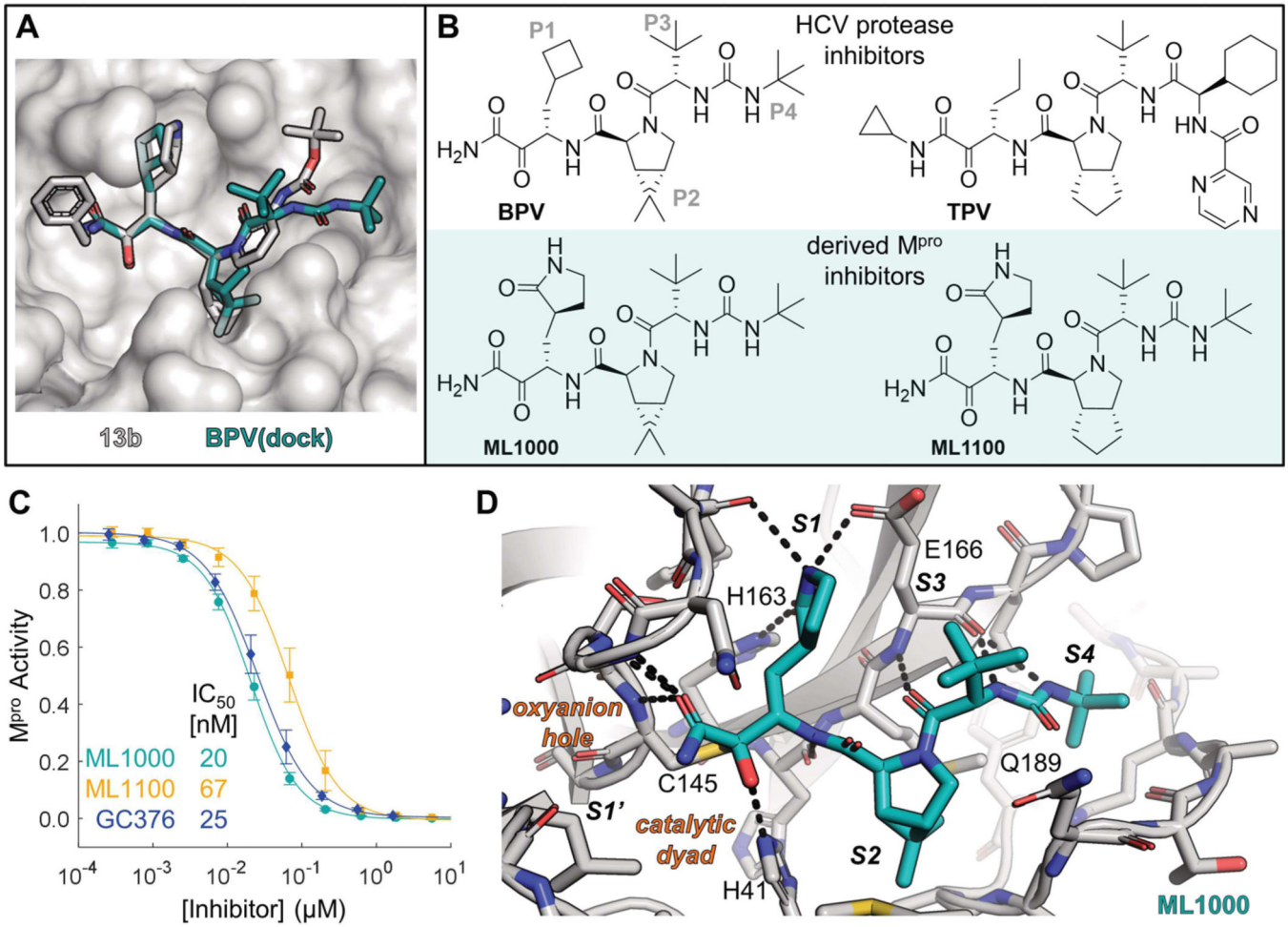

Fig. 1. M^{pro} inhibitor leads were derived from HCV protease inhibitors.

(**A**) Manual rigid docking of BPV into a 13b-M^{pro} co-crystal structure (PDB 6Y2G, protomer B). Using PyMOL, BPV was manually placed into the SARS-CoV-2 M^{pro} active site and unconstrained bonds were rotated for optimal complementarity. (**B**) Structures of BPV and TPV and the derived ML1000 and ML1100. ML1000 is essentially BPV with a P1 γ-lactam. ML1100 replaces the bicyclic P2 proline analog of BPV with that of TPV. (**C**) Inhibition of M^{pro}-coil activity by GC376, ML1000, and ML1100 at 25 °C after 1 h of preincubation. Data presented as mean ± SD. (**D**) Crystal structure of the ML1000-M^{pro} adduct with H-bond interactions highlighted with dashed lines. In (A) and (D), as well as representations of crystal structures in all following figures, oxygen, nitrogen, sulfur, and fluorine atoms are colored by a typical red, blue, yellow, and light blue color scheme, whereas carbon atoms are colored according to the chosen custom color scheme, for example teal for ML1000 in (D).

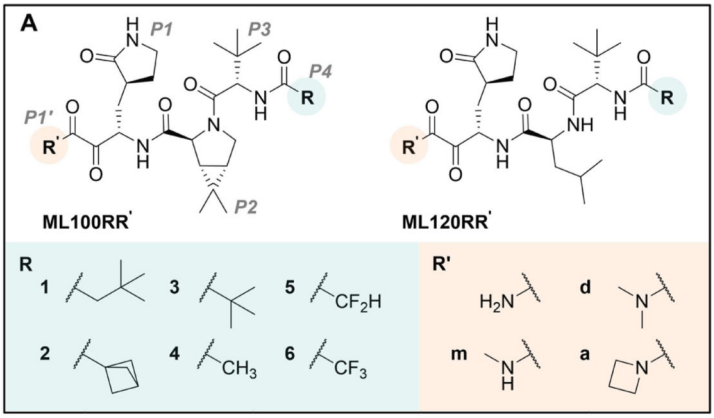

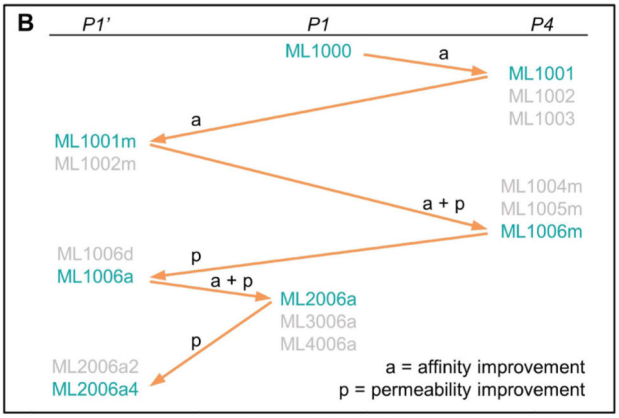

C

	IC_{50} (25 °C) M^{pro}-coil (nM)	$IC_{50,cell}$ Huh7 (μM)	$IC_{50}/IC_{50,cell}$ Permeability ratio	SARS-CoV-2 EC_{50} Huh7.5.1++ (μM)	SARS-CoV-2 EC_{50} A549+ (μM)
BPV	5900 (5500–6400)	n/a	n/a	~ 59	—
ML1000	20 (19–22)	n/a	n/a	>100	>100
ML1100	67 (58–77)	—	—	>100	>100
ML1001	13 (12–13)	2.6 (2.1–3.3)	0.005	~42	>100
ML1001m	6.0 (5.6–6.5)	13 (9–19)	0.0005	~54	—
ML1002	29 (27–31)	—	—	—	>100
ML1002m	14 (13–15)	—	—	—	>100
ML1003	44 (41–47)	—	—	—	>100
ML1004m	11 (10–12)	23 (17–31)	0.0005	—	—
ML1005m	3.4 (3.2–3.6)	1.7 (1.3–2.1)	0.002	~39	—
ML1006m	3.6 (3.4–3.8)	0.28 (0.22–0.35)	0.01	11 (7.7–15)	4.9 (4.0–6.0)
ML1006d	138 (130–145)	—	—	—	—
ML1006a	2.9 (2.7–3.1)	0.059 (0.047–0.075)	0.05	0.68 (0.55–0.85)	0.68 (0.59–0.78)
ML1201	18 (16–19)	—	—	—	—
ML1206m	6.5 (6.1–7.0)	0.83 (0.66–1.05)	0.007	—	—
GC376	25 (23–28)	0.16 (0.12–0.21)	0.16	0.13 (0.11–0.15)	4.1 (3.1–5.4)
NTV	2.2 (2.1–2.3)	0.15 (0.10–0.23)	0.01	0.19 (0.16–0.22)	0.10 (0.09–0.12)

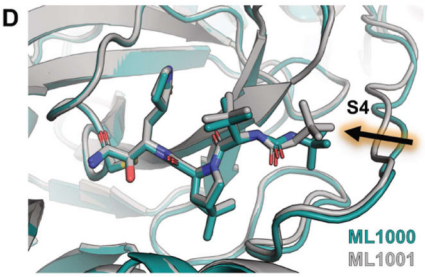

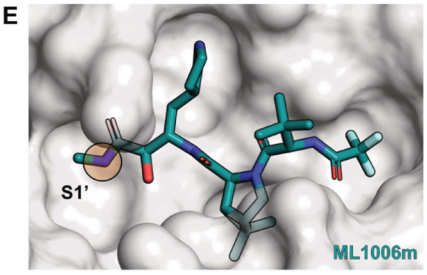

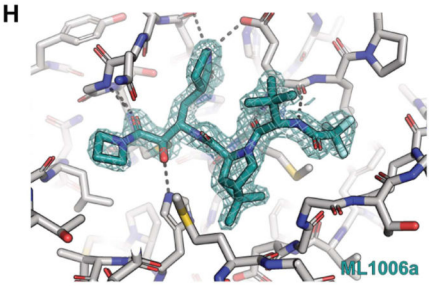

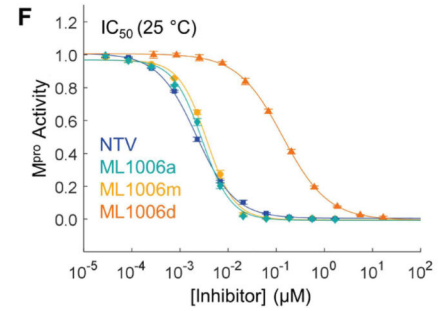

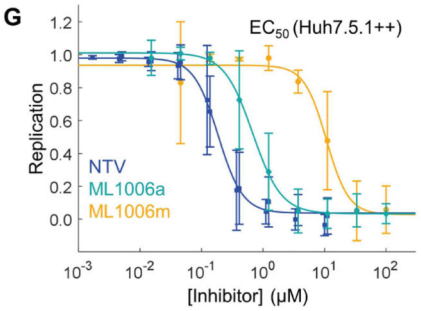

Fig. 2. Removal of H-bond donors improved permeability and potency.

(**A**) M^{pro} inhibitors based on ML1000. Additionally, select non-constrained inhibitors (P2 = Leu) were synthesized to assess the effects of P2 rigidification. (**B**) Progressing from ML1000, stepwise optimization of P4 (R), P1' (R'), and P1 was performed. (**C**) Inhibitor activity against purified M^{pro}-coil (IC_{50}), intracellular M^{pro} ($IC_{50,cell}$), and SARS-CoV-2 replication (EC_{50}). 95% confidence intervals (IC_{95}) are reported in parentheses and data, fits, and statistical details are found in fig. S4 to S7. IC_{50} data were measured at 25 °C after 1 h of preincubation. In contrast to NTV, the ketoamides have not reached equilibrium. n/a, not applicable. –, not available. (**D**) Co-crystals of M^{pro} with ML1000 or ML1001. The arrow indicates contraction of the S4 pocket for ML1001. (**E**) A M^{pro}-ML1006m co-crystal. The

circle highlights the position for N,N-substitution and extension of the ketoamide into S1'. (**F and G**) Inhibition curves for (F) M^{pro}-coil in solution and (G) SARS-CoV-2 replication in Huh7.5.1++ cells. Data are presented as mean ± SD. (**H**) Co-crystal of M^{pro}-ML1006a.

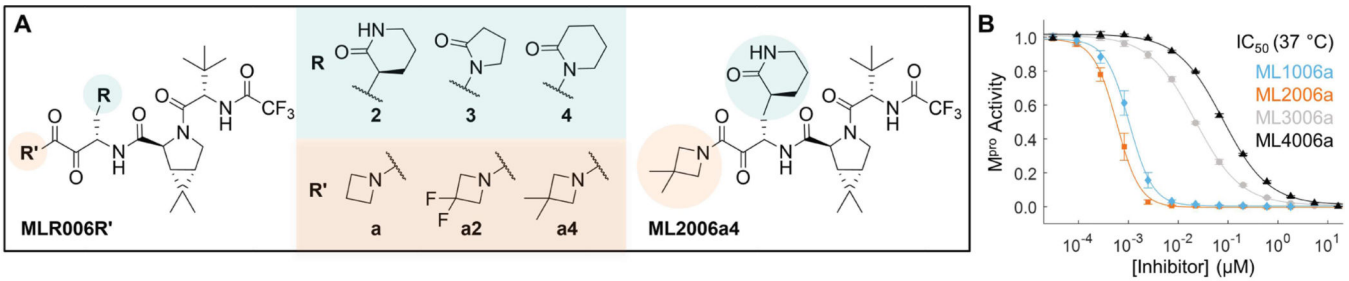

C

	IC_{50} (37 °C) M^{pro}-coil WT (nM)	K_i (37 °C) M^{pro}-coil WT (nM)	$IC_{50,cell}$ Huh7 (μM)	$IC_{50}/IC_{50,cell}$ permeability ratio	SARS-CoV-2 EC_{50} Huh7.5.1++ (μM)	SARS-CoV-2 EC_{50} A549+ (μM)
ML1006a	1.03 (0.98–1.08)	0.22 (0.19–0.26)	0.059 (0.047–0.075)	0.02	0.68 (0.55–0.85)	0.68 (0.59–0.78)
ML2006a	0.58 (0.55–0.62)	0.04 (0.01–0.08)	0.020 (0.013–0.030)	0.03	0.10 (0.07–0.14)	0.09 (0.08–0.12)
ML2006a2	0.77 (0.72–0.82)	0.06 (0.03–0.09)	0.006 (0.003–0.012)	0.13	0.12 (0.09–0.15)	0.14 (0.12–0.16)
ML2006a4	1.05 (1.00–1.10)	0.26 (0.22–0.30)	0.020 (0.014–0.028)	0.05	0.10 (0.07–0.13)	0.12 (0.10–0.14)
ML3006a	22 (21–23)	21 (19–22)	0.26 (0.16–0.42)	0.08	1.6 (1.4–1.7)	—
ML4006a	79 (74–84)	76 (72–81)	0.84 (0.58–1.22)	0.09	—	—
NTV	5.3 (5.0–5.6)	4.5 (4.3–4.8)	0.15 (0.10–0.23)	0.04	0.19 (0.16–0.22)	0.10 (0.09–0.12)
ETV	5.3 (4.8–5.8)	4.5 (4.1–5.0)	0.047 (0.037–0.058)	0.11	0.06 (0.05–0.08)	0.09 (0.07–0.12)
PTV	12 (11–13)	11 (10–12)	—	—	0.17 (0.14–0.21)	0.29 (0.22–0.37)

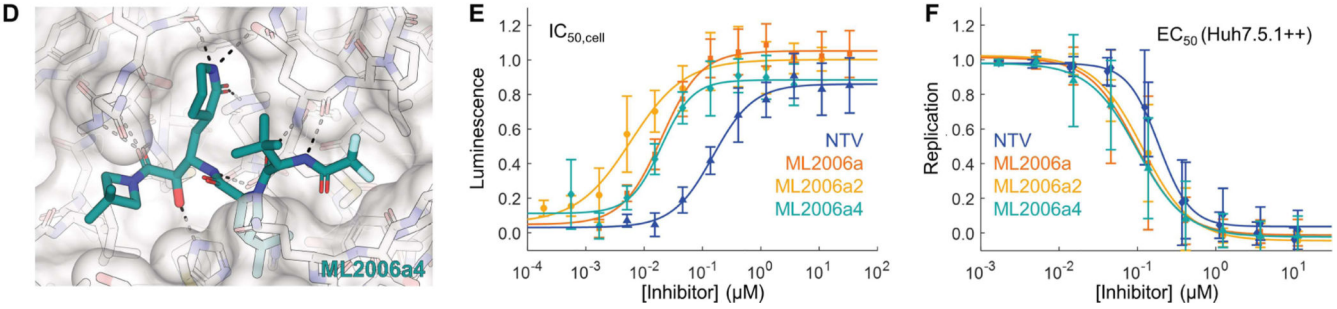

Fig. 3. SARS-CoV-2 M^{pro} inhibitors with higher in vitro potency than NTV were discovered. (**A**) P1 lactamyls and azetidine substitutions were tested to improve permeability. (**B**) IC_{50} curves are shown for ML1006a, ML2006a, ML3006a, and ML4006a. (**C**) Tabulation of inhibitor activity against purified M^{pro}-coil (IC_{50} and K_i), intracellular M^{pro} ($IC_{50,cell}$), and SARS-CoV-2 replication (EC_{50}). IC_{50} are reported in parentheses and data, fits, and statistical details are found in fig. S5, S6, S7, S9, and S13. IC_{50} and K_i data were measured at 37 °C after 3 h of preincubation to allow the equilibrium to settle for the ketoamides. –, not available (**D**) Crystal structure of the covalent adduct of ML2006a4 and SARS-CoV-2 M^{pro}. (**E**) Intracellular inhibition of M^{pro} ($IC_{50,cell}$) was measured using a luciferase proteolysis reporter. (**F**) Inhibition of SARS-CoV-2 replication in Huh7.5.1++ cell cultures by ML2006a derivatives. Data in (B), (E), and (F) are presented as mean ± SD.

A **Pharmacokinetics in male non-fasted C57BL/6 mice at 20 mg/kg in PDT formulation**

	$C_{max,u}$[a] (po) (μM)	$AUC_{\infty,u}$[a] (po) (ng·h/mL)	F[b] (po) (%)	CL_p[c] (iv) (mL·min^{-1}·kg^{-1})	V_{ss}[d] (iv) (L/kg)	c_{lung}/c_{plasma}[e] (po 8h)
ML1006m	0.06 ± 0.02	81 (41–114)	1.2 (0.5–2.0)	26 (23–31)	0.50 (0.45–0.57)	1.55 ± 0.01[g]
ML1006a	0.07 ± 0.02	76 (48–93)	2.8 (1.6–4.0)	41 (36–47)	0.69 (0.66–0.70)	1.09 ± 0.41[g]
ML2006a	0.06 ± 0.03	68 (45–91)	5.1 (2.8–8.6)	58 (48–75)	0.66 (0.57–0.77)	3.26 ± 2.6[f]
ML2006a4	0.39 ± 0.06	350 (297–403)	27 (20–36)	39 (34–46)	0.66 (0.61–0.72)	—
NTV	1.49 ± 0.10	839 (681–984)	24 (15–39)	23 (18–32)	0.51 (0.44–0.58)	0.32 ± 0.01
PTV	0.06 ± 0.01	44 (28–61)	31 (16–50)	30 (25–35)	3.0 (2.0–4.0)	—
RTV[f] + ML1006m	0.30 ± 0.13	742 (435–1049)	7.7 (4.1–12.1)	20 (18–23)	0.55 (0.52–0.56)	1.02 ± 0.68
RTV[f] + ML1006a	0.44 ± 0.07	1014 (656–1435)	19 (11–33)	21 (18–25)	0.84 (0.83–0.84)	1.44 ± 0.56
RTV[f] + ML2006a	1.23 ± 0.35	2736 (2005–3468)	59 (39–83)	17 (16–19)	0.89 (0.84–0.91)	0.69 ± 0.10
RTV[f] + ML2006a4	1.30 ± 0.08	5995 (4951–7038)	115 (86–151)	9.8 (8.9–10.9)	1.22 (1.15–1.31)	0.33 ± 0.01
RTV[f] + NTV	6.12 ± 0.65	14787 (12261–17312)	87 (70–106)	4.8 (4.1–5.7)	0.52 (0.47–0.57)	0.31 ± 0.05
RTV[f] + PTV	0.25 ± 0.18	894 (543–1245)	125 (51–328)	6.0 (4.1–11.4)	1.14 (0.93–1.22)	—

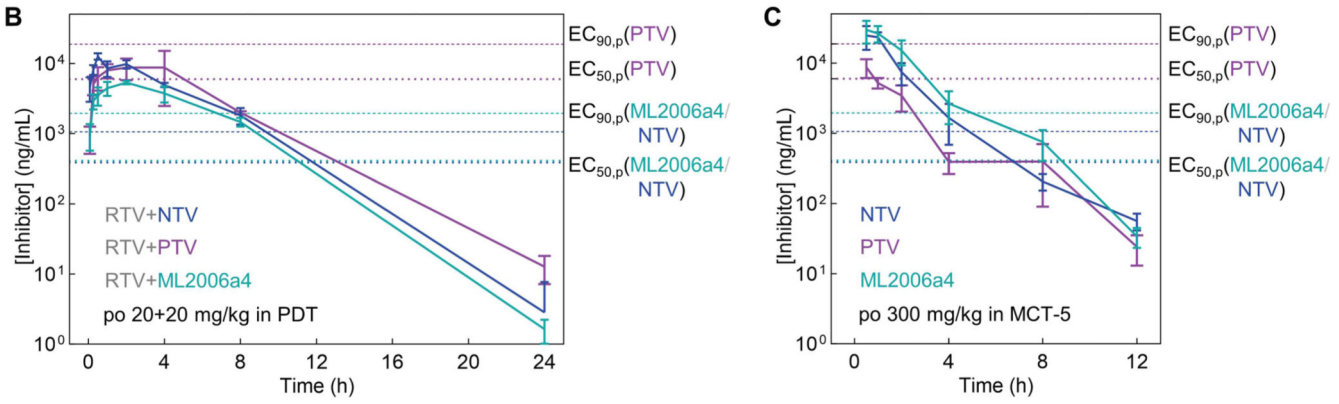

Fig. 4. ML2006a4 is orally bioavailable in mice.

(**A**) Key parameters from non-compartmental analysis of the mean inhibitor plasma concentration from pharmacokinetic studies performed in mice ($n = 3$) with oral (po) dosing at 20 mg/kg and intravenous (iv) dosing at 2 mg/kg in a saline solution with 40% PEG300, 10% DMSO, and 5% Tween-80 (PDT). In parentheses, uncertain estimates obtained as described in Materials and Methods. For direct experimental observations, mean ± SD are reported. [a]The unbound drug peak concentration ($C_{max,u}$) and area under the curve extrapolated to infinity ($AUC_{\infty,u}$) were calculated using f_u reported in table S1. [b]Oral bioavailability (F). [c]Plasma clearance rate (CL_p). [d]Volume of distribution at steady state (V_{ss}). [e]Ratio of inhibitor concentrations in lungs and plasma measured 8 h post oral dosing. [f]RTV dosed po at 20 mg/kg 30 min prior to test compound. [g] ($n = 2$) (**B**) Inhibitor plasma concentrations were monitored for 24 h after oral administration of a 20 mg/kg RTV pre-dose followed by single-doses of 20 mg/kg ML2006a4, NTV, or PTV solutions in PDT. (**C**) Inhibitor plasma concentrations were monitored for 12 h after single-agent oral administration of 300 mg/kg ML2006a4, NTV, or PTV suspensions in 0.5% methylcellulose and 5% Tween-80 (MCT-5). Data in (B) and (C) are presented as mean ± SD.

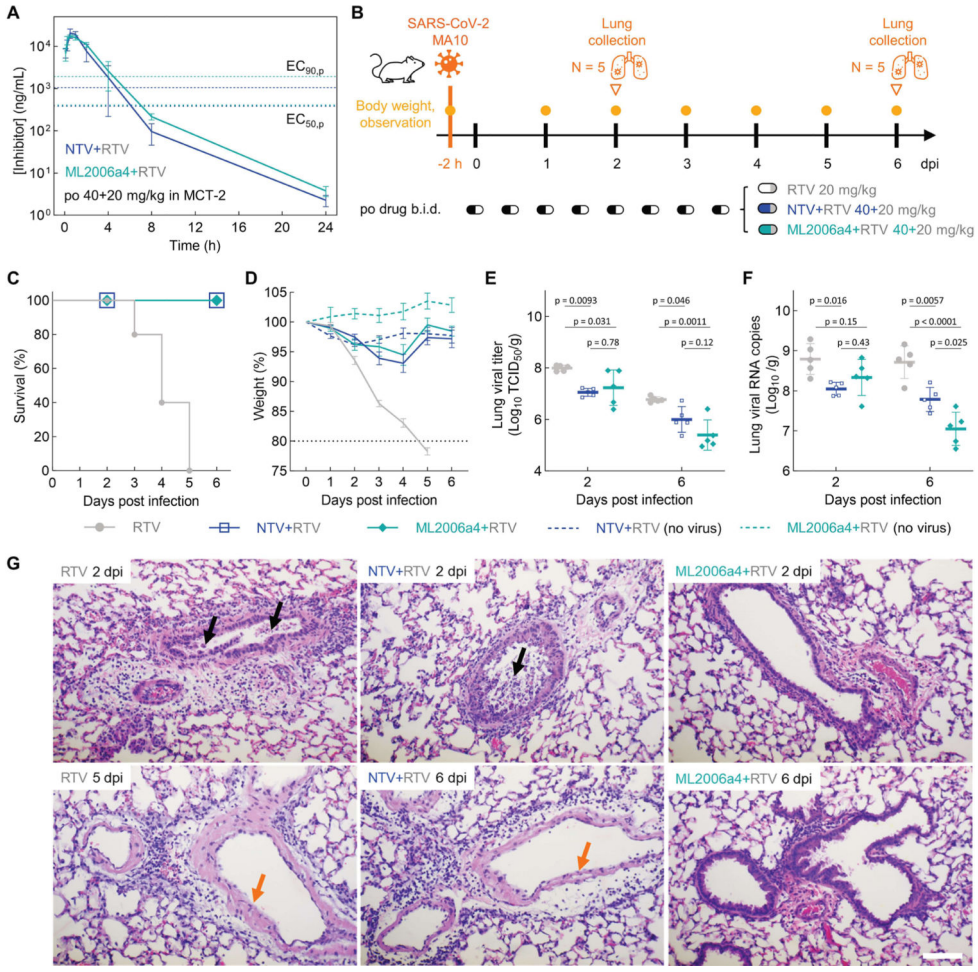

Fig. 5. ML2006a4 protects against SARS-CoV-2 in mice.

(**A**) Pharmacokinetics of the dosing regimen used for safety and efficacy testing in mice (n = 3). Plasma concentrations were monitored for 24 h after oral administration of co-suspensions of 40+20 mg/kg ML2006a4+RTV or NTV+RTV in 0.5% methylcellulose and 2% Tween-80 (MCT-2). (**B**) Protocol for efficacy testing of ML2006a4 in 16-week-old female BALB/c mice. After intranasal infection with SARS-CoV-2 MA10 (10^5 $TCID_{50}$), the mice received inhibitors po bid for 4 days. ML2006a4+RTV and NTV+RTV were dosed as in (A), and the RTV-only control was dosed at 20 mg/kg. All infected groups contained 10 mice with 5 mice euthanized at 2 dpi and 6 dpi, respectively. Uninfected control groups contained 5 mice that were euthanized at 6 dpi. (**C and D**) Daily survival curves (C) and body weights (D) are shown for all five groups. No death or clinical decline was observed for any of the ML2006a4+RTV or NTV+RTV treated groups. (**E and F**) Infectious viral titers (E) and viral RNA loads (F) were determined in lungs harvested at 2 and 6 dpi, respectively. For the RTV-only group, data plotted at 6 dpi are from lungs collected at death (actual time 3 to 5 dpi). (G) Representative images of H&E-stained lungs collected at 2 or 6 dpi. Scale bar indicates 80 μm. Histopathological analysis identified peribronchiolar and perivascular infiltrations with mononuclear cells and respiratory epithelial cell injury in the three infected groups. RTV and NTV+RTV groups exhibited a high extent of infiltrations

and severe injury in respiratory epithelia (black arrows, epithelial cell debris in the lumen) at 2 dpi followed by incomplete epithelial regeneration (orange arrows, missing epithelium) at 5 or 6 dpi. Data are presented as mean ± SD.

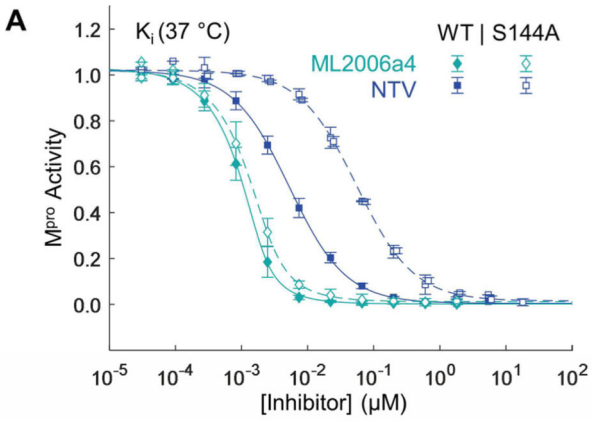

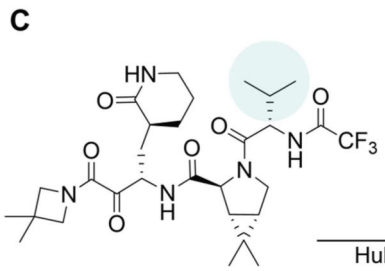

EC50 (μM)	
Huh7.5.1++	A549+
0.23 (0.17–0.31)	0.31 (0.24–0.39)

B

Ki (nM)
fold Ki increase over WT

	NTV	ETV	PTV	ML2006a	ML2006a4	ML2026a4
WT	4.5 (4.3–4.8) 1.0×	4.5 (4.1–5.0) 1.0×	11 (10–12) 1.0×	0.04 (0.01–0.08) 1.0×	0.26 (0.22–0.30) 1.0×	0.41 (0.34–0.48) 1.0×
S144A	55 (51–58) 12×	143 (129–156) 31×	103 (94–112) 9.3×	0.07 (0.01–0.12) 1.6×	0.63 (0.51–0.75) 2.4×	1.2 (1.0–1.3) 2.9×
L50F E166A	120 (108–131) 26×	136 (126–146) 30×	215 (198–232) 19×	0.51 (0.45–0.58) 12×	2.9 (2.6–3.3) 11×	4.8 (4.4–5.1) 12×
E166A	196 (180–211) 43×	255 (232–277) 56×	326 (299–353) 30×	0.80 (0.70–0.90) 19×	4.4 (3.8–5.0) 17×	8.8 (8.2–9.5) 21×
E166V	13000 (11000–15000) 2900×	308 (269–347) 68×	394 (367–421) 36×	19 (17–21) 450×	113 (98–128) 430×	28 (25–30) 67×
E166Q	22 (20–24) 4.8×	32 (29–35) 7.0×	44 (39–49) 4.0×	0.19 (0.13–0.24) 4.5×	1.1 (0.9–1.4) 4.3×	1.4 (1.2–1.6) 3.3×
A173V	59 (53–64) 13×	7.3 (5.8–8.7) 1.6×	44 (36–52) 4.0×	0.77 (0.61–0.92) 19×	3.6 (3.0–4.2) 14×	6.4 (5.6–7.3) 16×

Fig. 6. ML2006a4 exhibited improved mutation tolerance.

(**A**) Comparison of NTV and ML2006a4 in vitro inhibition curves against M^{pro}-coil WT and S144A. Data are presented as mean ± SD. (**B**) Inhibition constants, K_i, at 37 °C for M^{pro}-coil WT and six mutants. Colored numbers below represent fold change in K_i relative to WT M^{pro}. (**C**) EC_{50} values were determined for ML2026a4 that contains a smaller P3 group relative to ML2006a4. In (B) and (C), IC_{95} are reported in parentheses and data, fits, and statistical details are found in fig. S5, S6, S13, and S19.